JGR Space Physics

RESEARCH ARTICLE
10.1029/2021JA029465

Superposed Epoch Analysis of Nighttime Magnetic Perturbation Events Observed in Arctic Canada

Mark J. Engebretson[1], Lidiya Y. Ahmed[1,2], Viacheslav A. Pilipenko[1,3], Erik S. Steinmetz[1], Mark B. Moldwin[4], Martin G. Connors[5], David H. Boteler[6], James M. Weygand[7], Shane Coyle[8], Shin Ohtani[9], Jesper Gjerloev[9,10], and Christopher T. Russell[7]

[1]Department of Physics, Augsburg University, Minneapolis, MN, USA, [2]Now at NASA/Goddard Space Flight Center, Greenbelt, MD, USA, [3]Space Research Institute, Moscow, Russia, [4]Department of Climate and Space Sciences and Engineering, University of Michigan, Ann Arbor, MI, USA, [5]Athabasca University Observatories, Athabasca University, Athabasca, AB, Canada, [6]Geomagnetic Laboratory, Natural Resources Canada, Ottawa, ON, Canada, [7]Department of Earth Planetary and Space Sciences, University of California, Los Angeles, CA, USA, [8]Bradley Department of Electrical and Computer Engineering, Virginia Tech, Blacksburg, VA, USA, [9]Johns Hopkins University Applied Physics Laboratory, Laurel, MD, USA, [10]Department of Physics and Technology, University of Bergen, Norway

Key Points:

- Superposed epoch analyses of 2 years of >6 nT/s magnetic perturbation events (MPEs) from 5 high latitude Arctic stations are presented
- Of the solar wind and interplanetary magnetic field (IMF) parameters studied, only IMF Bz showed any consistent pattern: a drop and rise prior to MPE occurrence
- Most of the MPEs that occurred more than 30 min after a substorm onset did not coincide with peaks in the westward electrojet

Supporting Information:

Supporting Information may be found in the online version of this article.

Correspondence to:

M. J. Engebretson,
engebret@augsburg.edu

Citation:

Engebretson, M. J., Ahmed, L. Y., Pilipenko, V. A., Steinmetz, E. S., Moldwin, M. B., Connors, M. G., et al. (2021). Superposed epoch analysis of nighttime magnetic perturbation events observed in Arctic Canada. *Journal of Geophysical Research: Space Physics*, *126*, e2021JA029465. https://doi.org/10.1029/2021JA029465

Received 19 APR 2021
Accepted 9 AUG 2021

Abstract Rapid changes of magnetic fields associated with nighttime magnetic perturbation events (MPEs) with amplitudes |ΔB| of hundreds of nT and 5–10 min duration can induce geomagnetically induced currents (GICs) that can harm technological systems. Here we present superposed epoch analyses of large nighttime MPEs (|dB/dt| ≥ 6 nT/s) observed during 2015 and 2017 at five stations in Arctic Canada ranging from 64.7° to 75.2° in corrected geomagnetic latitude (MLAT) as functions of the interplanetary magnetic field (IMF), solar wind dynamic pressure, density, and velocity, and the SML, SMU, and SYM/H geomagnetic activity indices. Analyses were produced for premidnight and postmidnight events and for three ranges of time after the most recent substorm onset: (a) 0–30 min, (b) 30–60 min, and (c) >60 min. Of the solar wind and IMF parameters studied, only the IMF Bz component showed any consistent temporal variations prior to MPEs: a 1–2 h wide 1–3 nT negative minimum at all stations beginning ~30–80 min before premidnight MPEs, and minima that were less consistent but often deeper before postmidnight MPEs. Median, 25th, and 75th percentile SuperMAG auroral indices SML (SMU) showed drops (rises) before pre- and post-midnight type A MPEs, but most of the MPEs in categories B and C did not coincide with large-scale peaks in ionospheric electrojets. Median SYM/H indices were flat near −30 nT for premidnight events and showed no consistent temporal association with any MPE events. More disturbed values of IMF Bz, Psw, Nsw, SML, SMU, and SYM/H appeared postmidnight than premidnight.

1. Introduction

The threat to both spaceborne and ground-based technological systems posed by extreme events in Earth's space environment has led in recent years to numerous observational and modeling studies of the impact of dynamical processes in the solar corona that are conveyed to Earth via the solar wind plasma and interplanetary magnetic field that interact with Earth's magnetosphere and ionosphere.

The influence of extreme solar phenomena on Earth was first documented for the Carrington event of 1859 (Carrington, 1859), in which a large and complex set of solar flares caused not only widespread auroral displays but also disturbances in telegraph systems over a large portion of Earth. Observations of similarly rare events since then, such as recent studies of the great magnetic storms of May 1921 and March 1989 and their effects (Boteler, 2019; Hapgood, 2019; Love et al., 2019) have shown in more detail the ways in which "space weather" can have deleterious impacts on large-scale human technological systems, even to the extent of causing a blackout of the entire Hydro-Quebec electrical grid.

The mechanisms by which these externally driven events caused dangerous electrical currents at Earth's surface are now known to be rapid variations in Earth's geomagnetic field - large unipolar or bipolar solitary pulses predominantly in the premidnight sector or Pi3 or Ps6 pulsations in the postmidnight sector–with typical amplitudes |ΔB| of hundreds of nT and 5–10 min duration–(Belakhovsky et al., 2018; Boteler

et al., 1998; Engebretson et al., 2020; Viljanen, 1997; Viljanen et al., 2001; Vorobev et al., 2019; Yagova et al., 2018). Knipp (2015) presented an annotated bibliography of studies of these geomagnetically induced currents (GICs), and Ngwira and Pulkkinen (2019) provided an introduction to a collection of recent studies of GIC events. Improved understanding of the physical mechanisms that produce large, rapid, and localized variations in Earth's magnetic field has developed through both observational studies such as those cited above and through computer simulations (e.g., Honkonen et al., 2018; Marshalko et al., 2021; Mukhopadhyay et al., 2020; Welling et al., 2020; Wintoft et al., 2015). Recent efforts in the U.S. to support focused research, warning, and mitigation efforts have been documented by Knipp and Gannon (2019).

The regions in which most rapid variations in Earth's geomagnetic field are located are under the auroral zone, which is typically located between 60° and 75° in corrected geomagnetic latitude (MLAT). Because this "auroral oval" expands during major geomagnetic storms, large, rapid magnetic field perturbation events can extend to middle latitudes where denser networks of electrically conductive structures (high voltage power lines and pipelines) exist. The extreme events during which large magnetic perturbation events (MPEs) occur at middle latitudes are rather rare, and many observational and modeling studies of extreme MPEs have focused on these large geomagnetic storms or the substorms embedded within them. To date, however, a detailed understanding of the chain of physical processes that cause them remains elusive, and accurate predictions of their occurrence remain unattainable.

Viljanen and Tanskanen (2011), Engebretson, Pilipenko, et al. (2019) and Engebretson, Steinmetz, et al. (2019) have noted that extreme MPEs occur much more often at more typical auroral latitudes, so that a large set of such events can be compiled for detailed statistical and event studies, using data from arrays of ground-based magnetometers and auroral imagers. Three years ago we began a survey of >6 nT/s MPEs observed at high latitude stations during 2015 and 2017 in eastern Arctic Canada, part of 4 different magnetometer arrays. Any event with dB/dt > 5 nT/s is understood to be large enough to cause magnetic induction hazards (Boteler, 2001; Woodroffe et al., 2016), so these events (more than 50 per year at most of these stations) were all above the "danger" threshold. Although the high latitude sites in Arctic Canada used in this paper are not susceptible to GIC effects because of the absence of long electrical power lines or pipelines, the physical mechanisms involving transient ionospheric currents that produce MPEs and GICs are most likely to be the same under more expanded auroral oval conditions.

Two papers reporting results from this work were published in 2019 (Engebretson, Pilipenko, et al., 2019; Engebretson, Steinmetz, et al., 2019): the first paper presented statistical results using data from these magnetometers, and the second presented 3 case studies using auroral imagers and spacecraft data as well. A third paper (Engebretson et al., 2021, henceforth referred to as paper 3), as well as another study that compared MPEs observed in the Arctic and Antarctic using some of these stations as well as stations in Greenland (Engebretson et al., 2020), showed several differences in characteristics between premidnight and postmidnight MPEs. At least some of the postmidnight events were associated with auroral omega bands, as also noted by Viljanen et al. (2001) and Apatenkov et al. (2020).

In this study we build on the data base of large nighttime MPEs used in paper 3 to present a superposed epoch analysis of these MPEs as functions of the interplanetary magnetic field, the dynamic pressure, density, and velocity of the solar wind (from the OMNI database) time shifted to the nose of the Earth's bow shock, and the SML, SMU, and SYM/H geomagnetic activity indices. Because our previous studies noted that a substantial fraction of these events did not occur in close proximity to substorm onsets, analysis plots were produced separately at each station not only for premidnight and postmidnight MPEs, but also for three ranges of time after the most recent substorm onset: (a) 0–30 min, (b) 30–60 min, and (c) >60 min.

By providing detailed information on the temporal dependence of these events as functions of both external variables and geomagnetic activity indices, we provide statistical associations that may be helpful for understanding or at least circumscribing the physical mechanisms involved in their generation. Section 2 describes the data used in this study and the procedure used to identify and quantify MPEs. Sections 3 and 4 present superposed epoch analyses of each of the above external variables and of geomagnetic activity indices, respectively. Section 5 summarizes these observations and discusses their implications in the light of other recent studies, and Section 6 presents our conclusions and remaining open questions.

Table 1
Locations of the Magnetometer Stations Used in This Study

Array	Station	Code	Geog. lat.	Geog. lon.	CGM lat.	CGM lon.	UT of mag noon	Sampling rate (Hz)
MACCS	Repulse Bay	RBY	66.5°	273.8°	75.2°	−12.8°	17:47	2.0
	Cape Dorset	CDR	64.2°	283.4°	72.7°	3.0°	16:58	2.0
CANMOS	Iqaluit	IQA	63.8°	291.5°	71.4°	15.1°	16:19	1.0
AUTUMNX	Salluit	SALU	62.2°	284.3°	70.7°	4.1°	16:54	2.0
	Kuujjuarapik	KJPK	55.3°	282.2°	64.7°	0.2°	17:06	2.0

Note. CGM coordinates were calculated for epoch 2015, using http://sdnet.thayer.dartmouth.edu/aacgm/aacgm_calc.php#AACGM. Geographic and corrected geomagnetic (CGM) latitude and longitude are shown, as well as the universal time (UT) of local magnetic noon and the sampling rate.

2. Magnetometer Data Set and Prior Studies

Vector magnetometer data used in this study were recorded during 2015 and 2017 at five stations in the MACCS (https://doi.org/10.48322/sydj-ab90, Engebretson et al., 1995), CANMOS (Nikitina et al., 2016), and AUTUMNX (Connors et al., 2016) arrays in Arctic Canada with corrected geomagnetic latitude (MLAT) ranging from 64.7° to 75.2°, all within 1 h of the 0° magnetic meridian and sampling at 1 or 2 Hz, as detailed in Table 1 and Figure 1. The restriction of the data to two years in the declining phase of the solar cycle was based on data availability: full-year data from the AUTUMNX array were only available beginning in 2015, and during 2016 there was significant station down time at the two MACCS stations used in this study. Using a semi-automated process (described in detail in Engebretson, Pilipenko et al., 2019) we identified

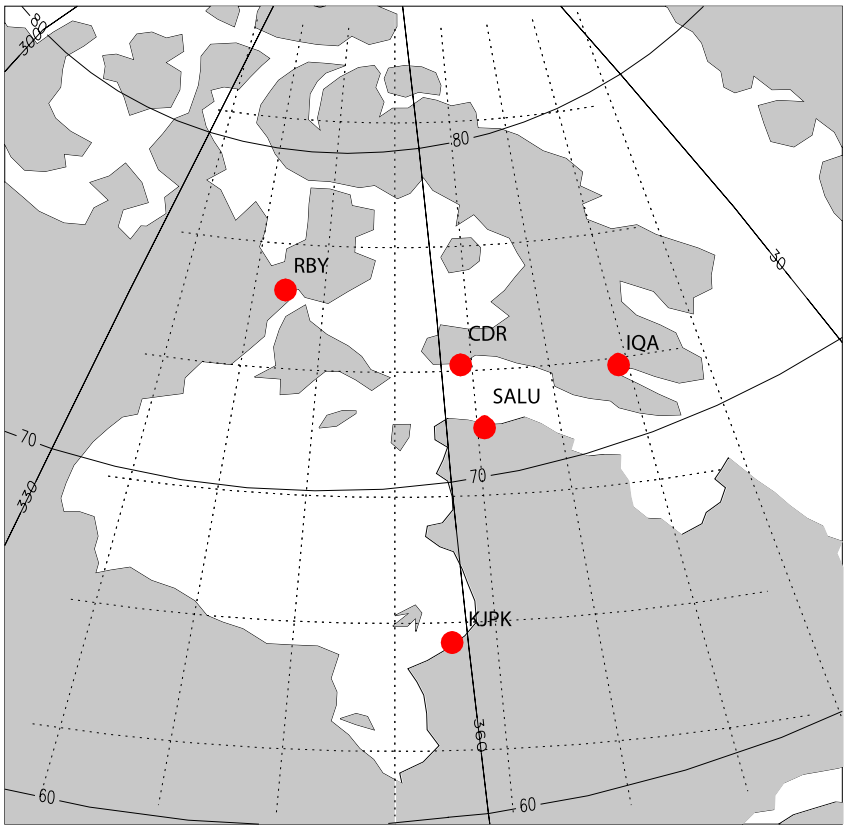

Figure 1. Map of ground magnetometer stations used for this study. Selected latitude and longitude lines in geomagnetic coordinates are shown. Station codes and their associated station names are listed in Table 1.

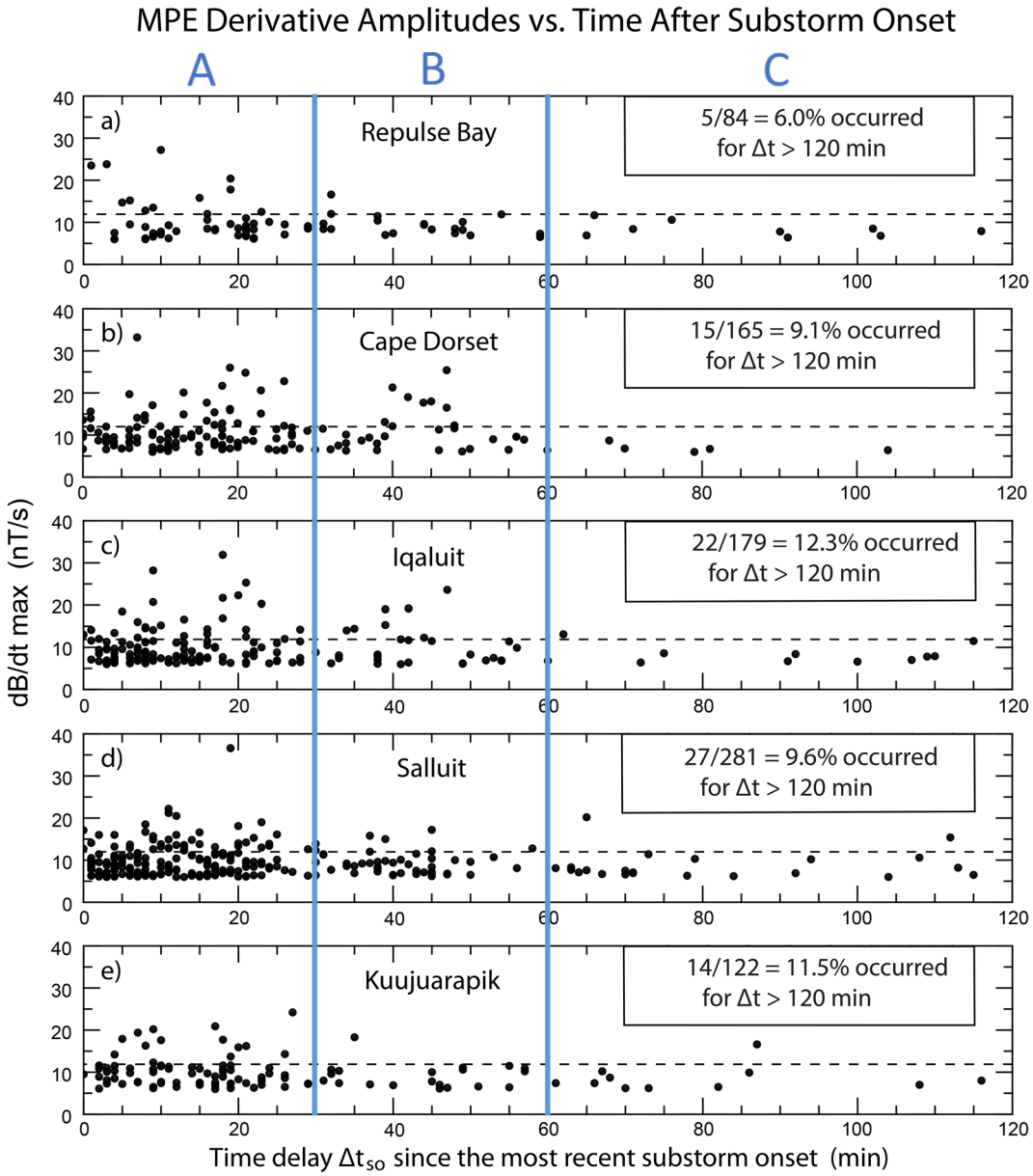

Figure 2. Plot of the amplitude of the maximum |dB/dt| value in any nighttime magnetic perturbation event (MPE) component observed at each station as a function of its delay Δt_{so} after the most recent substorm onset: (a) RBY, (b) CDR, (c) IQA, (d) SALU, and (e) KJPK. Only events with maximum derivative amplitude ≥6 nT/s are shown. The horizontal dotted line indicates an amplitude of 12 nT/s (from Engebretson et al., 2021).

all the MPEs with derivative amplitudes (|dB/dt| ≥ 6 nT/s). For each event we also recorded the values of the magnitude and vector components of the interplanetary magnetic field (IMF), solar wind pressure, number density, and speed, the SYM/H index, and the SuperMAG versions (SML and SMU) of the AL and AU auroral activity indices.

Figure 2, originally presented in paper 3, shows the number and amplitude of MPEs at each station as a function of their time delay after the most recent substorm onset (obtained from the SuperMAG substorm list using criteria detailed by Newell & Gjerloev, 2011). The total number of MPEs at each station ranged from 83 to 253, as detailed in Table 2. The two vertical blue bars separate the 3 time delay ranges. Roughly 10% of events at each station occurred more than 2 h after substorm onset.

Table 2
Distribution of "Pre- and Post-midnight" ≥6 nT/s MPEs at Each Station as a Function of Time Between the Most Recent Substorm Onset and Event Occurrence

	"Premidnight"									
	RBY		CDR		IQA		SALU		KJPK	
Station	#	%	#	%	#	%	#	%	#	%
Δtso ≤30 min	47	59	105	70	105	64	145	66	43	56
30 < Δtso <60 min	19	24	28	19	26	16	38	17	15	19
Δtso ≥60 min	13	16	18	12	32	20	39	18	19	25
Sum	79		151		163		222		77	
Combined: Δtso ≤30 min: 64% 30 < Δtso <60 min: 18% Δtso ≥60 min: 17%										
"Postmidnight"										
Δtso ≤30 min	3	75	5	56	7	70	18	56	31	74
30 < Δtso <60 min	1	25	3	33	3	30	7	22	5	12
Δtso ≥60 min	0	0	1	11	0	0	7	22	6	14
Sum	4		9		10		32		42	
Combined: Δtso ≤30 min: 66%, 30 < Δtso <60 min: 20%, Δtso ≥60 min: 14%										

Note. "Premidnight" MPEs include those observed between 1700 and 0100 MLT, and "postmidnight" events those between 0200 and 0700 MLT.
MLT, magnetic local time; MPEs, magnetic perturbation events.

All of the ≥6 nT/s perturbation events observed at these stations fell into the magnetic local time (MLT) range from 17 to 07 MLT. These events are displayed as a function of MLT in two ways in Figure 3 (also originally presented in paper 3). Figure 3a shows the number of occurrences of these MPEs at each station grouped in 1-h MLT bins and sorted by magnetic latitude. Different symbols are used to designate events based on the time of MPE occurrence after the closest prior substorm onset: plus signs for $\Delta t_{so} \leq 30$ min, open squares for Δt_{so} between 30 and 60 min, and open triangles for $\Delta t_{so} \geq 60$ min. Two populations are evident in this figure: a broad "premidnight" distribution extending from dusk to shortly after midnight (17–1 MLT) that appears at all latitudes shown, and a "postmidnight" distribution in the midnight to dawn sector (2–7 MLT) that is, prominent only at the lower latitude stations. The local time distributions in Figure 3a are consistent with the local time distribution of GICs in Figure 12 of Pulkkinen et al. (2003), which was based on an updated and extended version of the data originally presented by Viljanen et al. (2001). Both show two peaks: a broad premidnight one that extends to 1 MLT, and a smaller postmidnight one. The distribution of substorm onsets determined from IMAGE-FUV observations shown in Figure 2 of Frey et al. (2004) was similar to Figure 3a only in being confined to nighttime MLT hours; it was more tightly peaked between 21 and 01 MLT and had no secondary peak at later MLT.

Figure 3b shows the distribution of MPE derivative amplitudes (the maximum |dB/dt| during each event) at these same stations. MPE amplitudes were larger in the "premidnight" population at higher latitudes, but their amplitudes were similar in the two MLT ranges at the two lower latitude stations.

As Figure 3 shows, the number of "postmidnight" MPEs at the three most poleward stations was much lower than at the two more equatorward stations. Table 2 presents the numerical and percentage distributions of both "premidnight" and "postmidnight" MPEs in the six MLT and Δt_{so} categories used throughout this paper.

3. Superposed Epoch Analysis: External Influences

Because activity in Earth's magnetosphere is driven in large part by external influences, it has been helpful to investigate the time-dependent response of many magnetospheric phenomena such as geomagnetic storms, substorms, and various categories of wave phenomena to levels of and variations in the solar wind plasma and IMF that impinge on it. In this section we use the superposed epoch technique (Chree, 1913; Lühr et al., 1998) to investigate both the levels and temporal variations of the dynamic pressure (Psw),

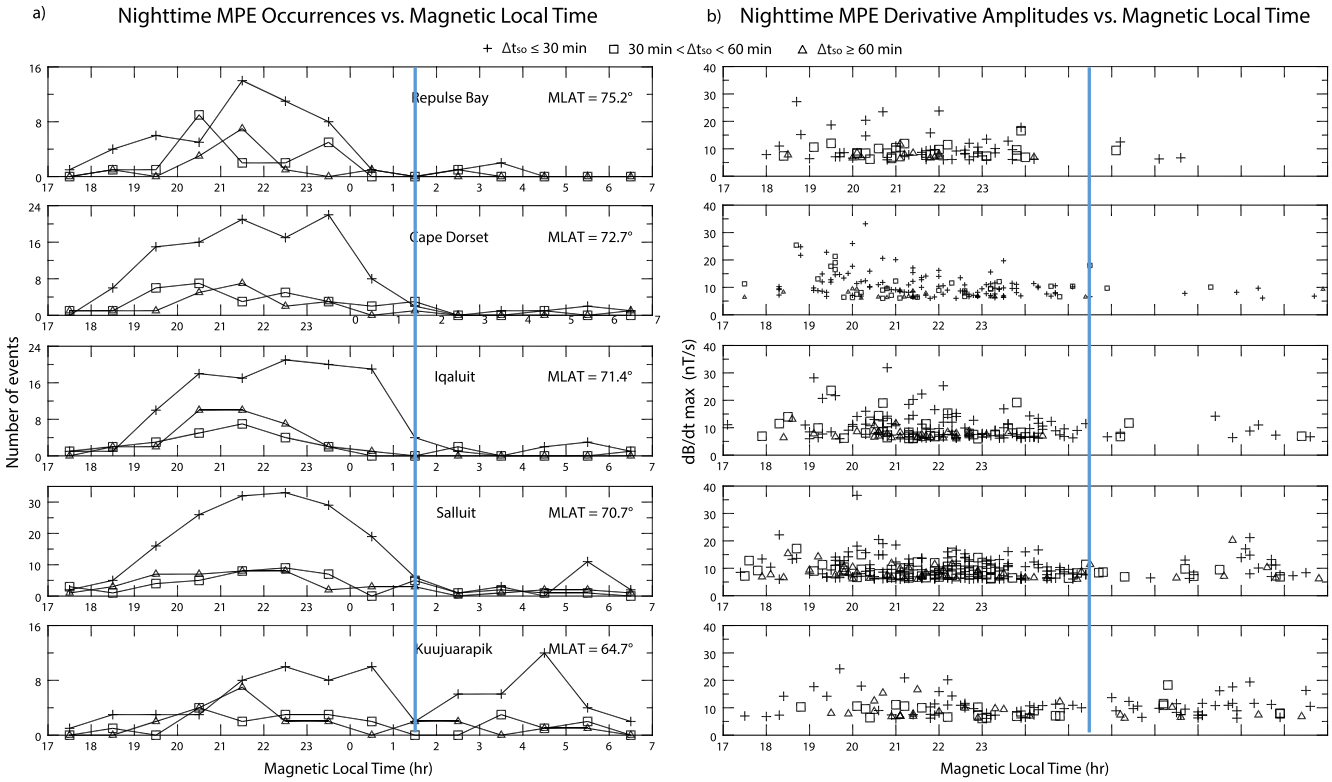

Figure 3. Panel a shows the number of occurrences of ≥6 nT/s nighttime magnetic perturbation events (MPEs) observed at RBY, CDR, IQA, SALU, and KJPK in 1-h bins of magnetic local time (MLT) from 17 to 07 h, sorted by each station's magnetic latitude. The vertical scale is different for each station. Panel b shows the distribution of MPE derivative amplitude at these same stations, with a uniform vertical scale. Different symbols are used to designate events based on the time of MPE occurrence after the closest prior substorm onset: plus signs for $\Delta t_{so} \leq 30$ min, open squares for Δt_{so} between 30 and 60 min, and open triangles for $\Delta t_{so} \geq 60$ min (from Engebretson et al., 2021).

number density (Nsw), and velocity (Vsw) of the solar wind, and the magnitude |B| of the IMF, its individual components Bx, By, and Bz in the GSM (geocentric solar magnetic) coordinate system, and its azimuthal angle in the ecliptic plane.

Each superposed epoch plot in Sections 3 and 4 shows the value of a given external variable over an 8-h period, from 4 h before the occurrence of an MPE to 4 h afterward. Plots with only black traces show median values at each station for MPE events in each of the six MLT and Δt_{so} categories described above (no plots are shown if the number of events in a given category was less than 5). Color plots, presented for selected stations and/or categories, show all instances of the given variable or index as thin black traces, as well as their median (yellow) and 25th and 75th percentiles (red).

3.1. Solar Wind Pressure, Density, and Velocity

Figure 4 shows median values of the solar wind dynamic pressure Psw for all five stations and in all six categories for which the number of events was ≥5. Median Psw values were nearly flat between 2 and 3 nPa for all 3 premidnight categories, slightly larger than the two-year median Psw value of 1.95 nPa. Postmidnight median Psw values were larger (3 to nearly 15 nPa), more variable (partly because of the smaller number of events in panels b6-b7 and c6-c7), and exhibited a slight increase 30–120 min prior to $t = 0$ for events in categories A and B.

Medians of Psw, however, do not convey information about the distributions of their values; in nearly every subcategory shown in Figure 4 at least one Psw trace had values exceeding 10 nPa. Figure 5 shows two such examples, corresponding to panels a2 and a5 of Figure 4. Although most MPEs occurred when Psw values

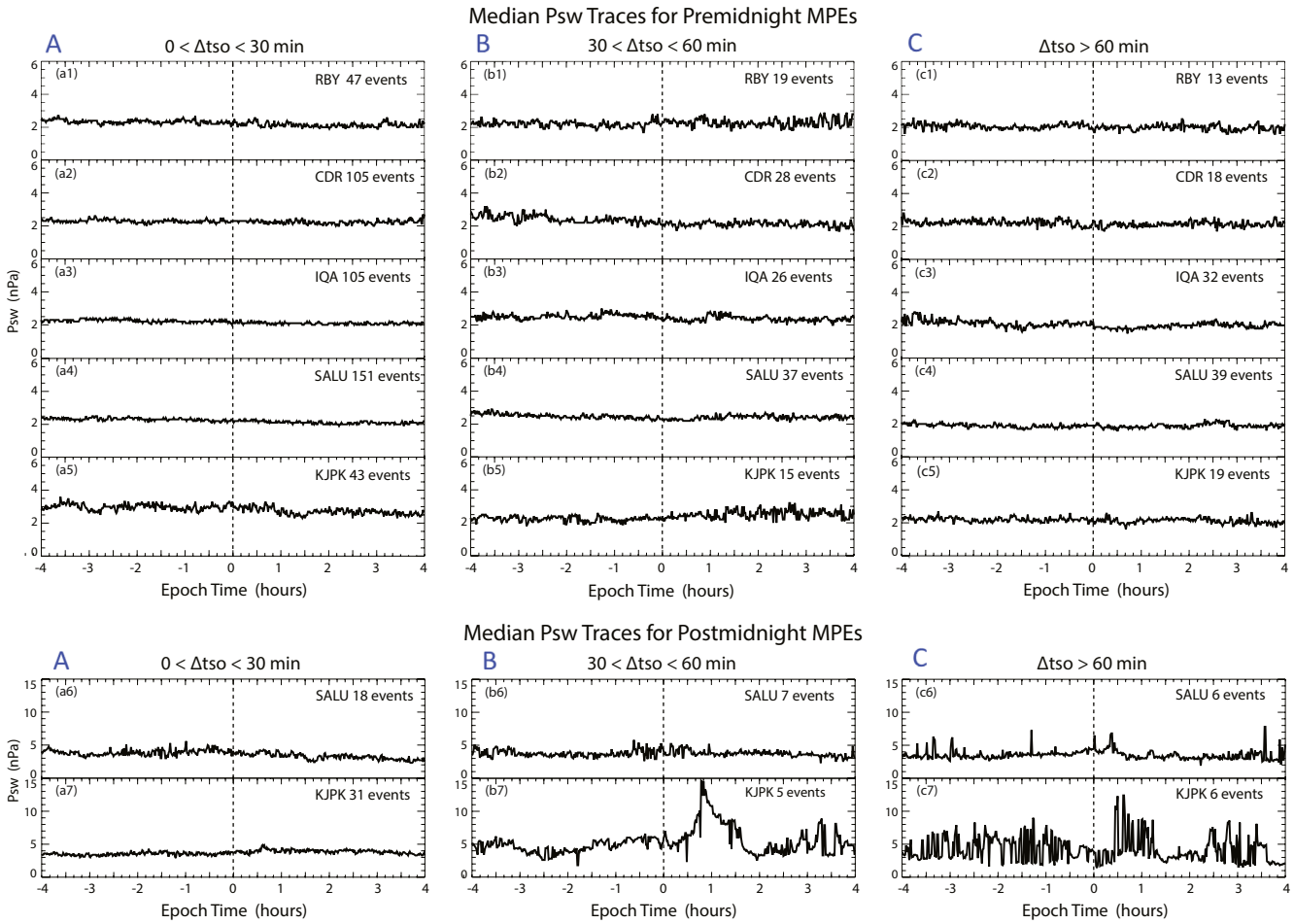

Figure 4. Superposed epoch plots of the medians of solar wind pressure dynamic pressure (Psw) as a function of time from 4 h before to 4 h after the time of magnetic perturbation events (MPEs). Premidnight panels a1–a5, b1–b5, and c1–c5 show medians for each of the 5 stations in the three Δt_{so} time delay ranges A, B, and C. Postmidnight panels a6–a7, b6–b7, and c6–c7 show corresponding medians for the two lowest latitude stations. Note the change of vertical scale for postmidnight events.

were near or only slightly above the yearly mean, a small number occurred during intervals of large and highly fluctuating Psw that revealed no consistent temporal pattern.

Plots analogous to those in Figures 4 and 5 are presented in Figures S1 and S2 for Nsw and Figures S3 and S4 for Vsw, respectively. These also show nearly flat medians for all 3 premidnight categories and somewhat more variable medians for postmidnight categories.

Figure S1 shows that median Nsw values were nearly flat from 4 h before to 4 h after premidnight MPE occurrences at all five stations, and their range, from 3.5 to 5.5 cm^{-3}, was centered on the two-year median value of 4.5 cm^{-3}. For the considerably fewer postmidnight events (most at lower latitude), median Nsw values were higher (5–8 cm^{-3}) and more variable but exhibited no consistent temporal pattern. Figure S2 shows example plots of all Nsw traces during category A events at CDR and KJP. The distribution of events was similar to that for Psw: a few highly variable traces that exceeded 20 cm^{-3} were observed, but many more traces remained below 3 cm^{-3} and were nearly steady.

Figure S3 shows that median Vsw values were between 450 and 650 km/s at all stations both premidnight and postmidnight (somewhat above the two-year median Vsw value of 422 km/s). These again showed no trends during the 8-h interval about premidnight MPEs at the three most poleward stations, but with slight gradual drops at the two lowest latitude stations. Postmidnight Vsw values were again more variable but with no consistent temporal pattern. Figure S4 shows example plots of all Vsw traces during category A

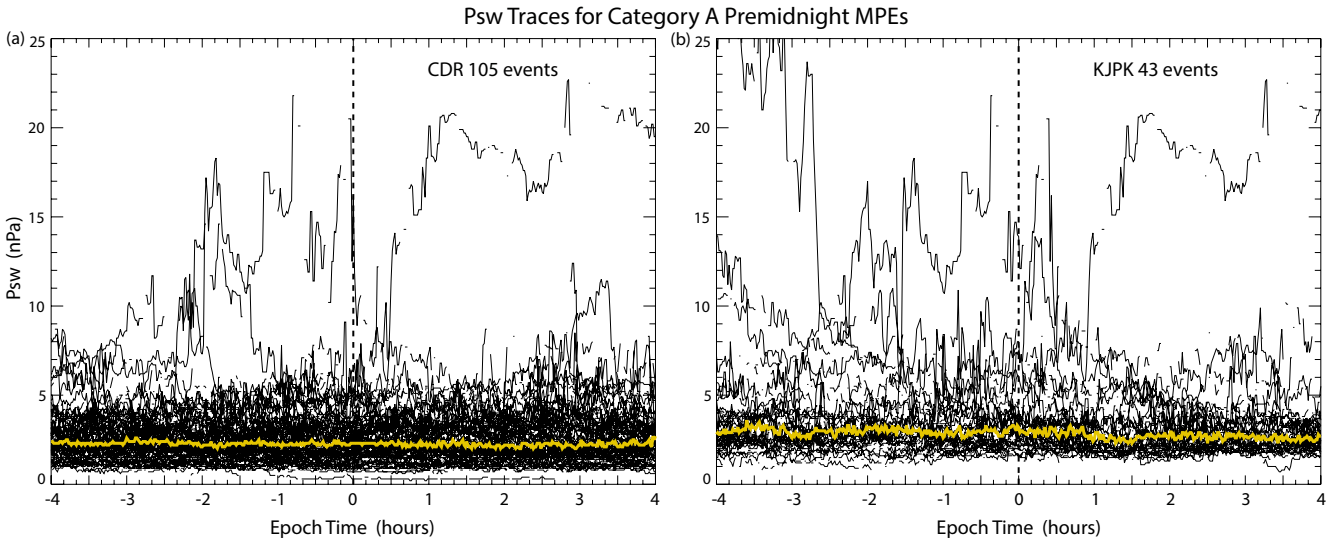

Figure 5. Superposed epoch plots of all events (black traces) and the median (yellow trace) of solar wind pressure dynamic pressure (Psw) as a function of time from 4 h before to 4 h after the time of premidnight MPEs in time delay range A from (a) CDR and (b) KJPK.

events at CDR and KJPK. Very few Vsw traces exceeded 700 km/s, and again these revealed no consistent temporal pattern; most of the individual traces shown were rather flat over the 8-h interval. Figure S4b shows a gap in Vsw traces near 550 km/s, which is partly obscured by the yellow median trace. One puzzling detail is that occurrence minima such as this, in the velocity range from ~500 to 600 km/s, appeared at several stations and in several event categories (not shown). We do not yet have an explanation for this gap.

3.2. Interplanetary Magnetic Field

Of the solar wind and IMF parameters studied, only IMF Bz showed any consistent pattern prior to MPE occurrence. Figure 6 shows that premidnight median Bz values in categories A and B at all 5 stations had a 1–2 h wide 1–3 nT negative minimum beginning ~30–80 min before $t = 0$ and rising to or beyond $t = 0$. The minima did not correspond to the time of substorm onset. Negative medians preceded premidnight category C events as well, but they were nearer 0 nT at the two higher latitude stations, and were successively more negative with lower latitude. Median minima that were less consistent but often deeper preceded postmidnight MPEs

Plots from two representative stations showing all Bz traces (Figures 7 and 8) indicate that this pattern held for the 25th and 75th percentile traces in most cases as well as for the medians, but that not every Bz trace was negative prior to MPE occurrence or showed a similar time dependence. Very similar patterns held for the all-trace Bz plots for the other three stations as well (not shown).

In contrast to the substantial negative excursions of IMF Bz medians prior to MPE occurrences in most panels of Figure 6, fewer identifiable patterns appeared in superposed epoch plots of IMF Bx and By. Figures S5 and S6, in the same format as Figure 6, show the median traces of IMF Bx and By for all six MLT and time delay categories. Premidnight category A panels showed a 1–2 nT rise and slight fall in Bx during the 4 h before MPE occurrence and a corresponding 1–2 nT fall and slight rise in By, but no consistent pattern was evident in most panels prior to postmidnight MPEs or later premidnight MPEs. The magnitudes of both Bx and By were also somewhat larger for postmidnight than premidnight events (note the larger vertical scales).

Figure 9 shows superposed epoch plots of all IMF Bx and By values and the median and 25th and 75th percentiles in premidnight category A MPEs observed at CDR. The traces for both components were centered roughly near 0, but the median in Bx was <0, and that in By was >0, consistent with a Parker-Spiral oriented IMF vector directed toward Earth. However, the IMF Bx and By traces in Figure 9 also show a large range of values, both positive and negative, such that the 25th and 75th percentiles have opposite signs. Examination

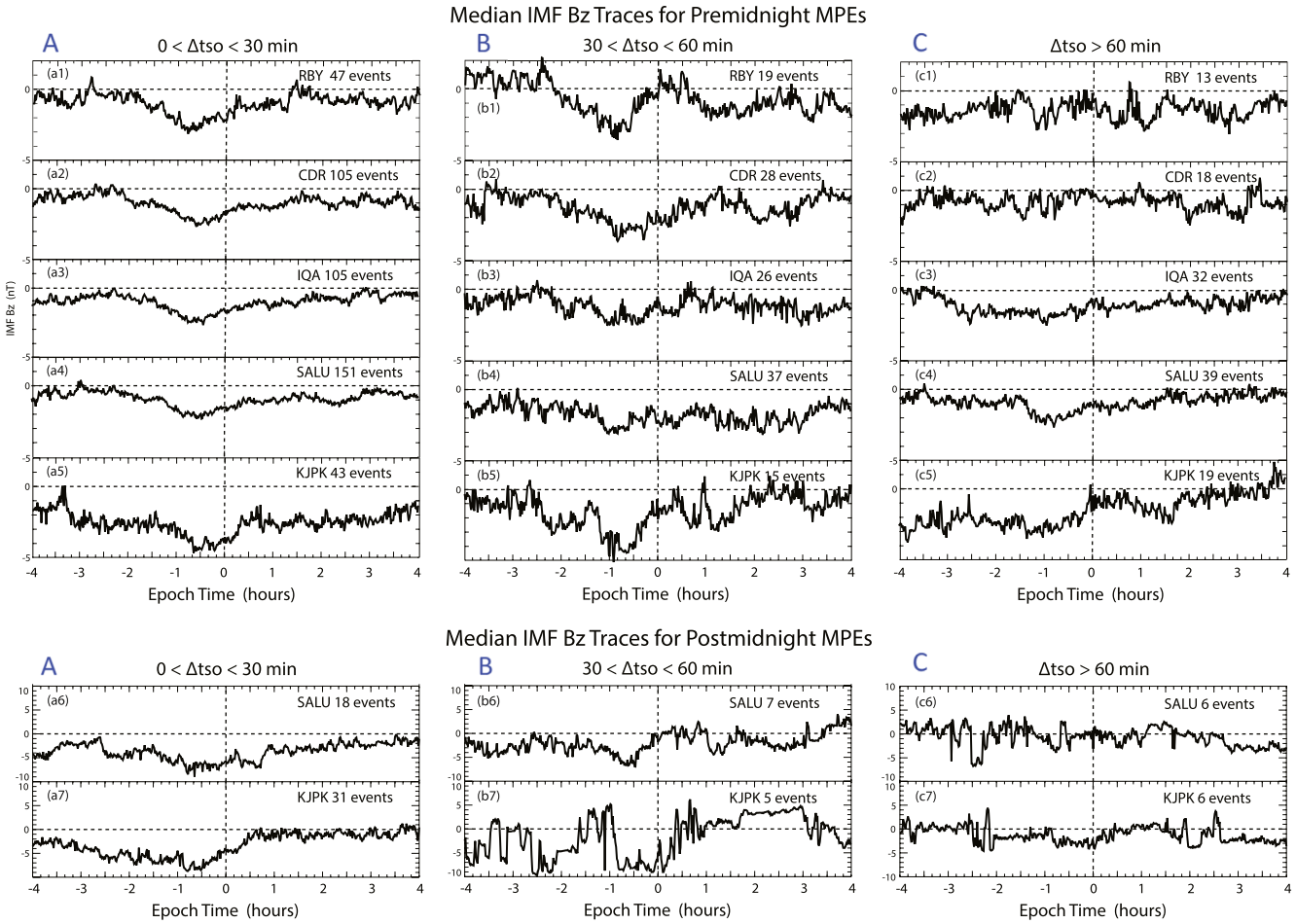

Figure 6. Superposed epoch plots of the medians of the north-south component of the interplanetary magnetic field (IMF Bz) as a function of time from 4 h before to 4 h after the time of magnetic perturbation events (MPEs), as in Figure 4.

of similar plots of Bx and By traces at all five stations and all six categories (not shown) revealed that the 25th and 75th percentile traces had opposite signs for most or all of the 8 h interval in nearly every case.

Figure S7 shows the medians of the *x*–*y* vector component of the IMF (in the ecliptic plane) for all six MLT and time delay categories. A Parker-Spiral orientation directed Earthward was observed consistently for category A premidnight events (panels a1-a5) and was often observed during category B premidnight events (panels b1–b5), but the directions were much more varied and at times had ortho-Parker-Spiral orientation for category C premidnight events (panels c1–c5) and for all postmidnight events (panels a6–a7, b6–b7, c6–c7). The median IMF orientation during premidnight category A and B events was not only in the Parker-spiral direction, but was also oriented predominantly in the direction toward Earth. The implications of these patterns are unclear, but may provide clues for further study. The magnitudes of postmidnight median vectors were also larger than premidnight ones, consistent with the larger medians in Bx and By.

In order to determine the influence of large IMF By events on MPE occurrence, we compared 156 events during 2015 compiled by Shane Coyle of Virginia Tech (doi:10.5281/zenodo.4657235) when the IMF vector was within ±30° of the GSM *Y*-axis, |By|was >6 nT, and events lasted longer than 30 min, to the times of MPE occurrences at 3 stations during that year. Only one of these MPEs (62 at CDR, 67 at IQA, and 71 at KJPK) occurred during the time of the large IMF By events. This suggests that MPEs require IMF conditions prior to or during their occurrence that are dominated by negative IMF Bz, and thus any effects of large IMF By orientations to promote asymmetry between hemispheres might not apply strongly to these nighttime impulsive events, and may in fact suppress the magnetotail instabilities that appear to be the cause of these events.

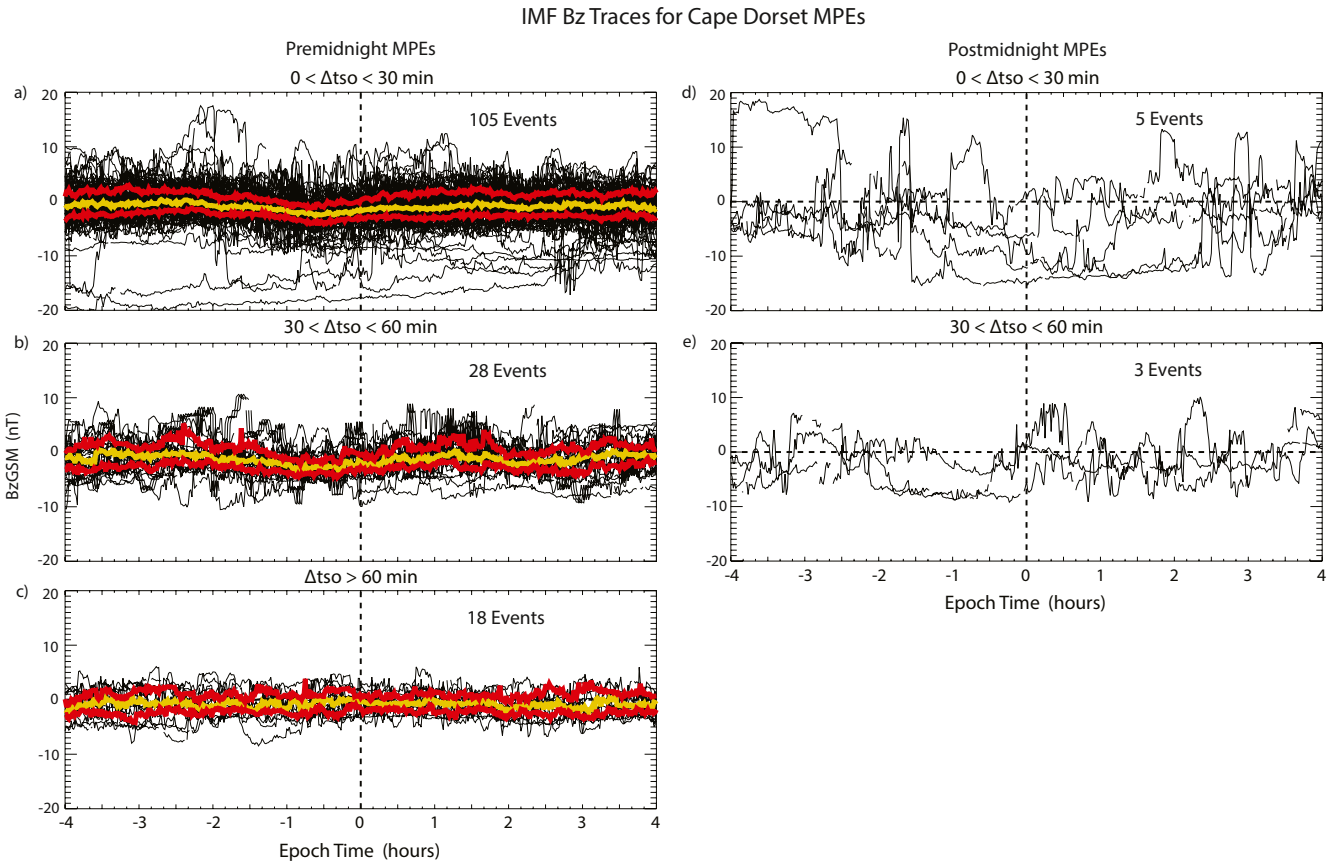

Figure 7. Superposed epoch plots of all interplanetary magnetic field (IMF) Bz traces (black), the median (yellow), and the 25th and 75th percentiles (red) as a function of time from 4 h before to 4 h after the time of premidnight magnetic perturbation events (MPEs) in all available time delay and magnetic local time (MLT) categories observed at CDR. No medians or percentile traces are shown when the number of events ≤6.

Figure S8 shows that median IMF |B| values were nearly flat from 4 h before to 4 h after premidnight MPE occurrences at all five stations; there was no consistent pattern to the small deviations observed at the two stations with the smallest numbers of events (RBY and KJPK). Premidnight median |B| values were between 5 and 6 nT at the four most poleward stations (only slightly higher than the two-year median |B| value of 5.16 nT) and somewhat higher at KJPK (between 5 and 8 nT). In contrast, median |B| traces for postmidnight MPEs were more variable and dropped gradually from between 8 and 12 nT to between 5 and 8 nT during the 8-h interval. Figure 10, which shows plots of all IMF|B|traces for category A premidnight MPEs at CDR and KJPK, again indicates the wide range of IMF magnitudes and the lack of any consistent temporal patterns before, during, and after MPEs occurring within 30 min of substorm onsets. A similarly wide range of magnitudes was observed at each station and in all six categories.

4. Superposed Epoch Analysis: Geomagnetic Activity Indices

Because geomagnetic activity indices are derived from previous or at best near real time observations of activity such as geomagnetic storms or substorms, they of course cannot be used as predictors of such activity. However, superposed epoch plots of global indices may reveal temporal patterns in activity that can aid in understanding the causal chain leading to their occurrence. In this section we present such plots for three indices: SME, SML, and SYM/H.

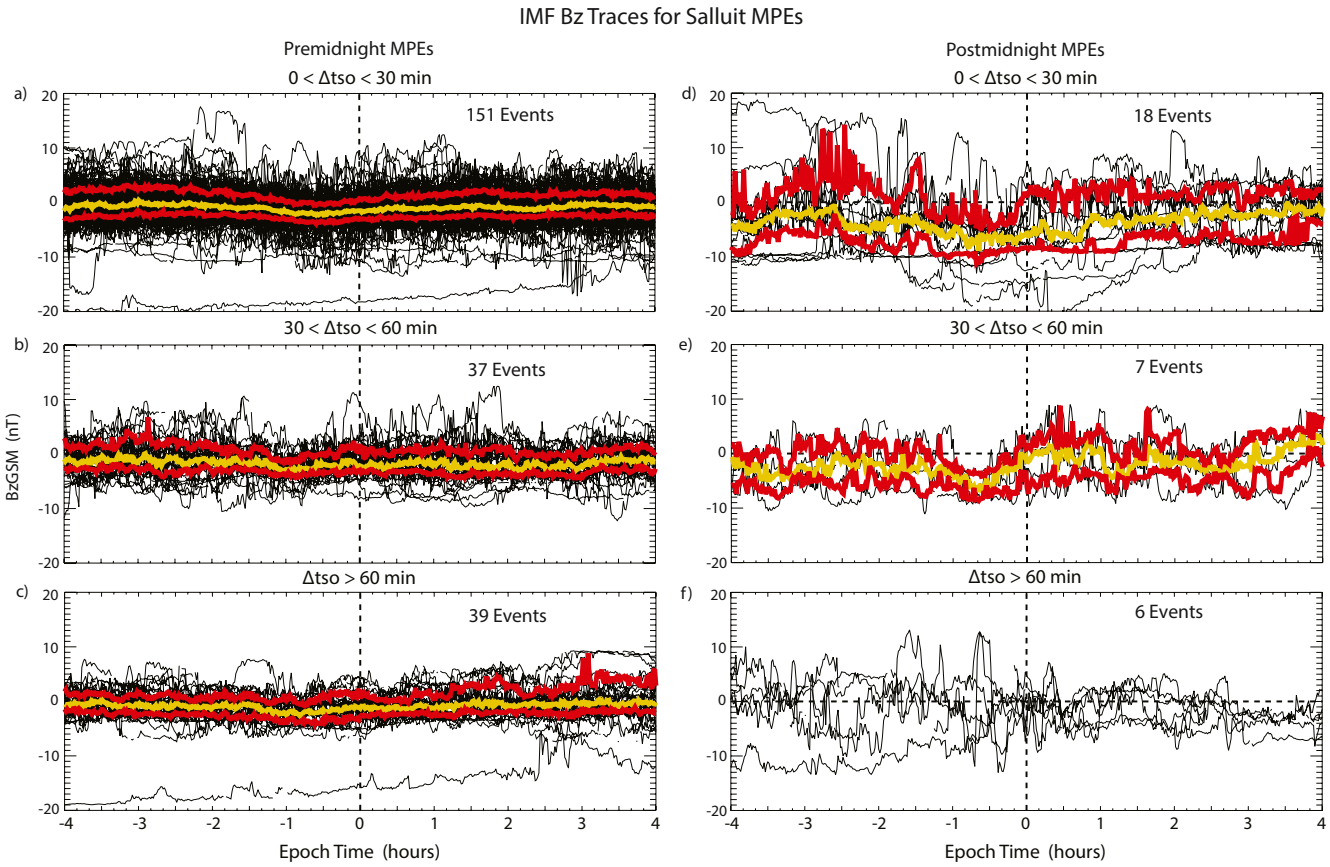

Figure 8. Superposed epoch plots of all interplanetary magnetic field (IMF) Bz traces (black), the median (yellow), and the 25th and 75th percentiles (red) as a function of time from 4 h before to 4 h after the time of premidnight MPEs in all available time delay and magnetic local time (MLT) categories observed at SALU. No medians or percentile traces are shown when the number of events ≤6.

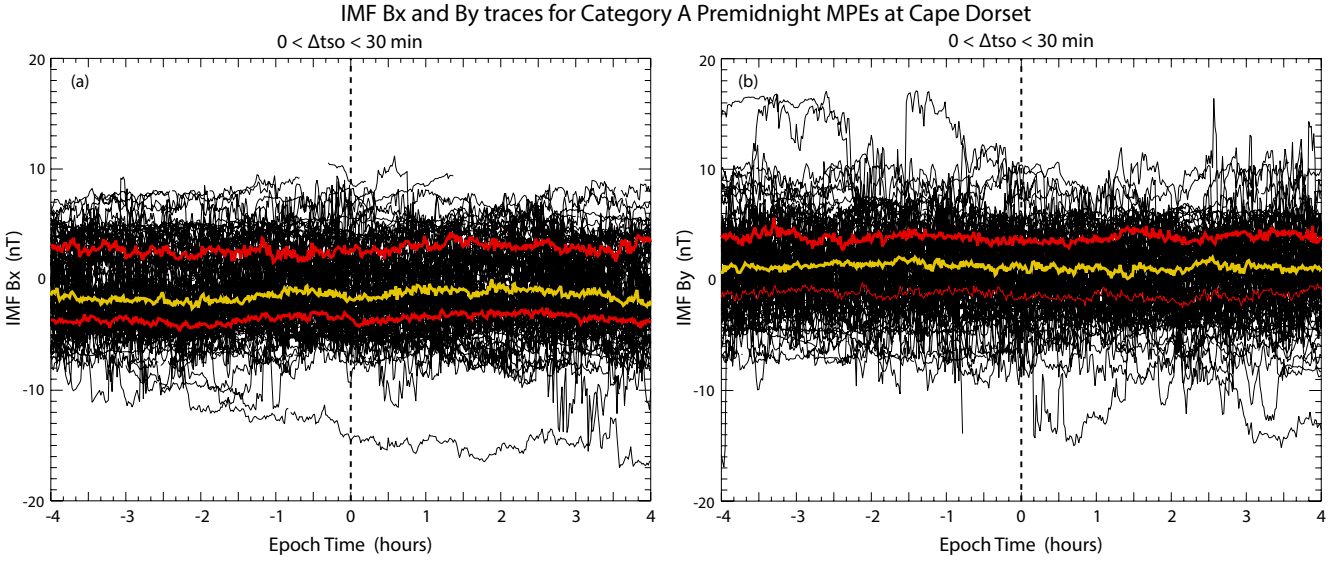

Figure 9. Superposed epoch plots of all interplanetary magnetic field (IMF) Bx (panel a) and By (panel b) values (black traces), the median (yellow traces), and the 25th and 75th percentiles (red traces) as a function of time from 4 h before to 4 h after the time of premidnight category A magnetic perturbation event (MPEs) observed at CDR.

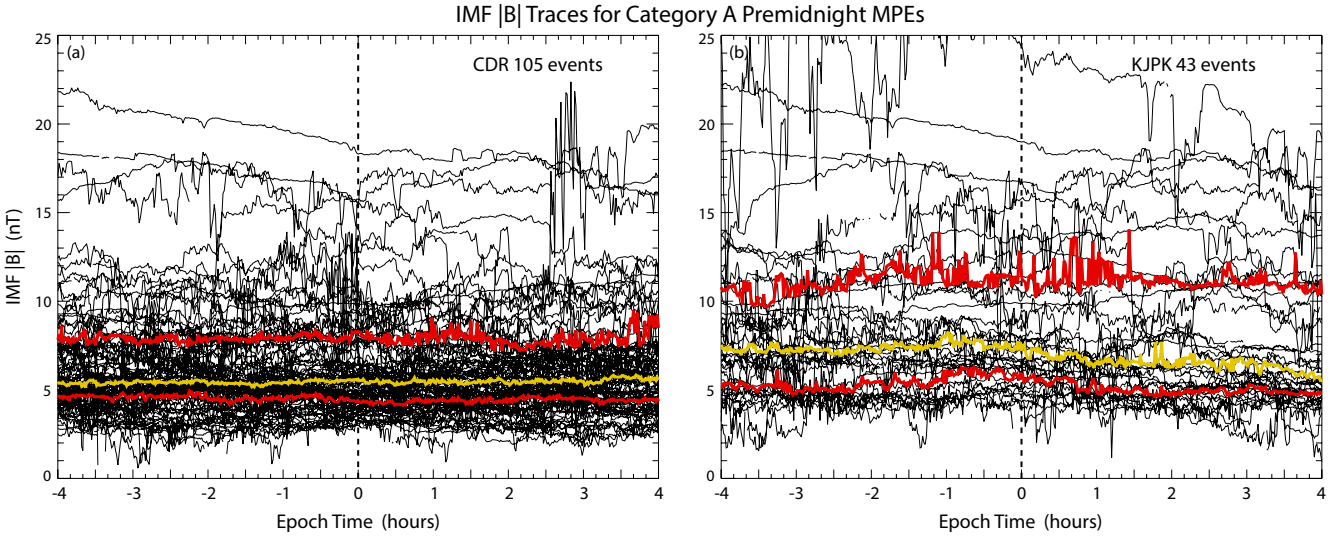

Figure 10. Superposed epoch plots of all interplanetary magnetic field (IMF) |B| values (black traces), the median (yellow traces), and the 25th and 75th percentiles (red traces) as a function of time from 4 h before to 4 h after the time of premidnight category A magnetic perturbation event (MPEs) observed at (a) CDR and (b) KJPK.

4.1. SML and SMU

Like the more traditional AL and AU auroral electrojet indices, the SuperMAG versions of the these indices, SML and SMU, respectively, measure aspects of auroral power (Newell & Gjerloev, 2011), but they are based on data from a much larger set of ground observatories. SML and SMU measure the strength of the westward (eastward) electrojet, respectively, and rapid and moderately sustained decreases in SML are used to identify substorm onsets.

Figures 11 and 13 show superposed epoch plots of all SML and SMU values, respectively, as well as medians and 25th and 75th percentiles from CDR, SALU, and KJPK. Similar plots from RBY and IQA closely resembled those from CDR (not shown).

Superposed epoch traces of the SML index showed the largest variety of behavior as a function of category of any parameter studied here. Panels a1–a3, b1–b3, and c1–c3 of Figure 11 show that a wide range of SML values for premidnight events at each station appeared throughout the 8-h periods shown, with a large number of values near 0 both before and after $t = 0$ but also with some large negative values, extending to even −1,600 nT, in most panels. However, very similar temporal patterns appeared in the median and both the 25th and 75th percentile traces of category A premidnight events (panels a1-a3): a modest slow rise from −4 to −1.5 h was followed by a much steeper decrease with increasingly negative slope from −1.5 h to $t = 0$ h, with a median amplitude drop of ∼400 nT. After a more gradual rise after $t = 0$ SML values returned to earlier levels after ∼2 h. The full width–half minimum duration of the premidnight SML category A medians was ∼50 min. Many individual SML traces were complex (with multiple subsidiary peaks), but the fwhm duration of their individual peaks often ranged between 15 and 40 min.

The minima of a large number of individual traces occurred between ∼−15 min and +30 min, suggesting that many of the MPEs in this category coincided approximately with the times of the most intense westward electrojets. It is consistent with the time delays shown in Figure 2 that only a few MPEs coincided with onsets (0–30 min prior), which are associated with rapid but step-like drops in SML.

Figure 12 provides a zoomed-in histogram view of the distribution of minima in each SML trace at CDR and KJPK in the range from −30 to +30 min epoch time for category A premidnight events. Panel (a) shows a nearly symmetric distribution at CDR between −5 and +5 min and peaked at 0 min, with very few events beyond ±10 min. Panel (b) shows a distribution that was skewed 2–3 min toward later times but again had very few events beyond ±10 min. Both panels confirm that MPEs and minima in SML during category A premidnight events very often occurred within ∼10 min of each other, but also shows that they were only

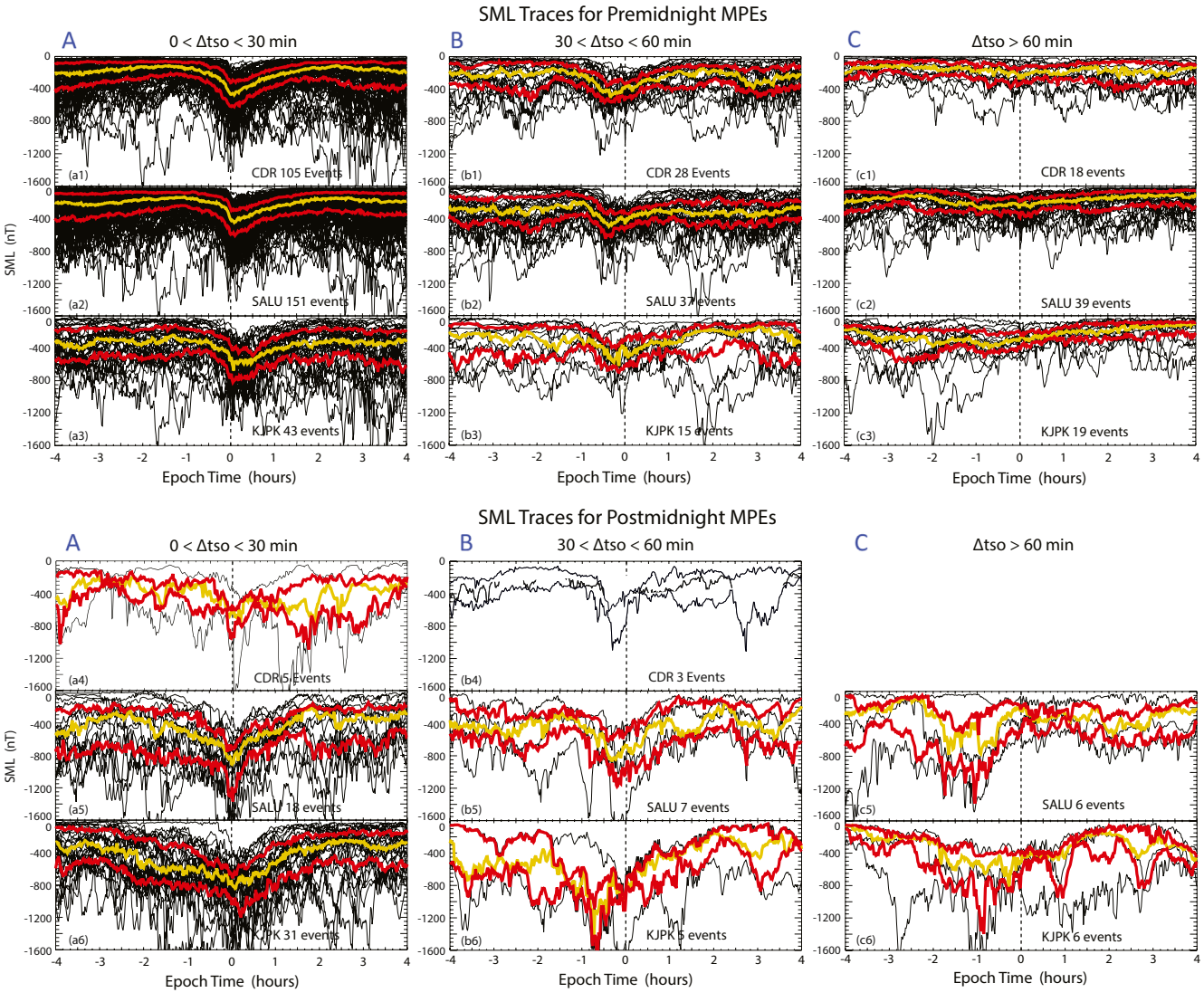

Figure 11. Superposed epoch plots of all SML index values (black traces), the median (yellow traces), and the 25th and 75th percentiles (red traces) as a function of epoch time in all six magnetic local time (MLT) and Δt_{so} categories of magnetic perturbation event (MPEs) observed at CDR, SALU, and KJPK.

occasionally simultaneous. This time range is consistent with observations that large MPEs often occur during the downward (upward) slopes before (after) the times of minima of 5–10 min duration negative spikes in Bx (cf. example event waveforms in Figures 3, 6 and 9 of Engebretson, Steinmetz, et al., 2019).

Panels b1–b3 of Figure 11 show that for category B premidnight events minima in the medians and 25th and 75th percentile traces occurred ~30 min before $t = 0$ at CDR and SALU, and 15–25 min at KJPK, so most of these MPEs did not coincide with peaks in the westward electrojet or with substorm onsets. Very few large negative peaks appeared in the traces in panels c1–c3 for category C premidnight events, and none of the most negative ones occurred near $t = 0$. The traces, median, and the 25th and 75th percentile traces in these panels also were much less variable than those for categories A and B events.

Panels a4–a6 and b4–b6 of Figure 11 shows that postmidnight SML temporal patterns at each station were similar to their premidnight counterparts in each category, but with ~2 times more negative values. They also showed much more variability, due in part to the smaller number of postmidnight events at each station. In contrast to the relatively flat premidnight category C panels c1–c3, postmidnight panels c5–c6 showed large negative peaks for ~2 h prior to $t = 0$ and occasional large negative peaks throughout the 8-h period shown. The medians and both percentiles tended toward 0 nT from −1 h to slightly past $t = 0$, again

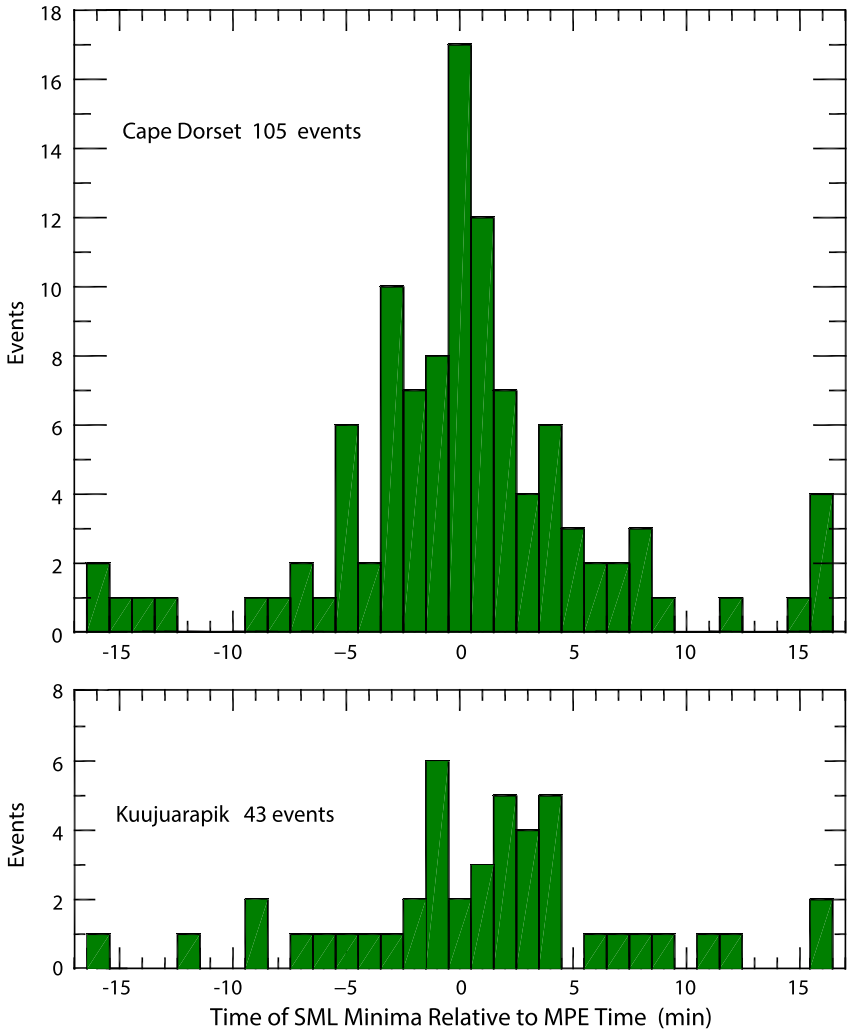

Figure 12. Plot of the relative time between SML minima and magnetic perturbation event (MPE) occurrences for premidnight category A MPEs observed at (a) CDR and (b) KJPK during 2015 and 2017. Bars to the left of −15 indicate the number of events between −30 and −16 min, and bars to the right of +15 indicate the number of events between +16 and +30 min.

suggesting little or no temporal correlation between these MPEs and simultaneously increased electrojet activity. Premidnight median minima were deeper for category A MPEs than for premidnight categories with larger time delays, but postmidnight minima in the median and both percentiles were at some stations deepest for categories with larger time delays, but as noted above the latter minima did not occur at $t = 0$.

We further note that those SML traces in premidnight panels a1–a3 of Figure 11 that were near 0 nT prior to $t = -5$ min dropped sharply by $t = 0$. Similar drops began slightly earlier in premidnight panels b1–b3, and all of the SML traces in postmidnight panels a4–a6 and b4–b6 dropped to below −200 nT by $t = 0$. These rapid drops may reflect the rapid development of the localized currents that drive MPEs. Of course, based on this information alone one cannot distinguish between currents that are stationary (but with amplitudes rapidly changing in time) from rapidly moving current structures that may have more constant amplitude. A denser array of ground stations and a different type of analysis would be needed to distinguish between these two extremes.

The SMU traces in Figure 13 showed less temporal variability than SML traces, but their maxima also varied in time relative to MPE occurrence for categories A, B, and C. Premidnight category A SMU traces (panels a1–a3) peaked 10–15 min after the MPEs, while rises in category B traces were broader in time and reached

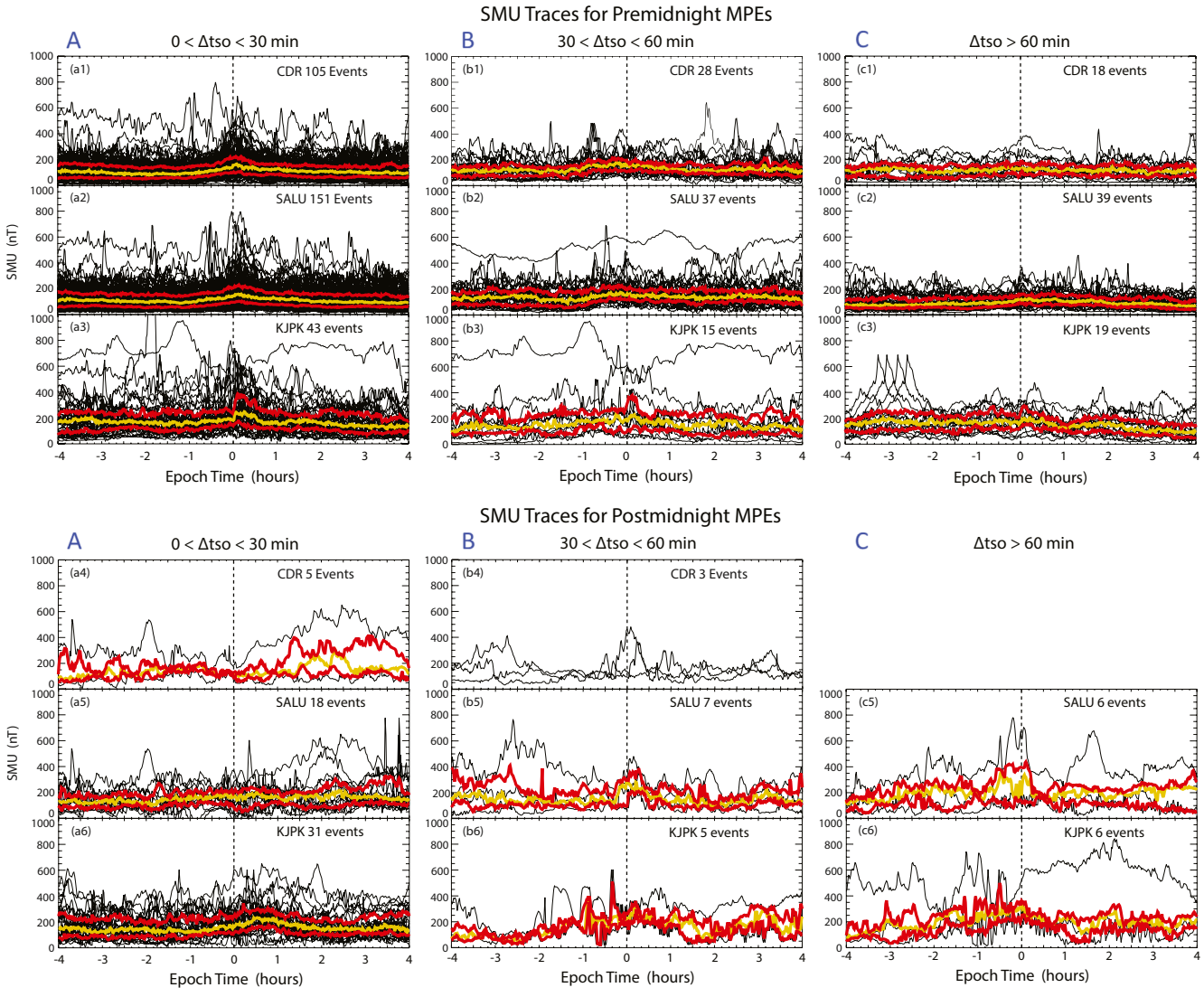

Figure 13. Superposed epoch plots of all SMU index values (black traces), the median (yellow traces), and the 25th and 75th percentiles (red traces) as a function of epoch time in all six magnetic local time (MLT) and Δt_{so} categories of magnetic perturbation event (MPEs) observed at CDR, SALU, and KJPK.

their maximum values 15–20 min before the MPEs, and category C traces at 2 of the 3 stations shown maximized from 10 to 40 min after the MPEs. The postmidnight patterns for SMU also differed considerably from those for SML. Whereas panels a4–a6 of Figure 11 showed SML minima in medians and both 25th and 75th percentiles at $t = 0$, the median SMU traces in panels a4–a5 of Figure 13 were essentially flat, and the trace in panel a6 had a modest peak centered at $t = +30$ min. Peaks in median SMU values appeared in panels b4–b6 and c5–c6 of Figure 13 at or slightly after $t = 0$, while minima in median SML values appeared from 15 to 45 min before $t = 0$ in panels b4–b6 of Figure 11, and only weakly in panels c5–c6. This difference in the timing of several peaks in SML and SMU in postmidnight category B and C events (the peaks in SMU were closer in time to $t = 0$ than the minima in SML) suggests that at least some of these MPEs may have been associated with eastward electrojets. The relative amplitude of increases of peaks in median SMU values in panels b4–b6 and c5–c6 in Figure 13, however, were similar to the relative amplitude of decreases of peaks in median SML in panels b4–b6 and c5–c6 of Figure 11. The behavior of the SML and SMU traces in category A near 0 nT before $t = 0$ also differed: Nearly all SML traces in panels a1–a6 of Figure 11 dropped to −150 nT or below at $t = 0$, but the lowest SMU traces in panels a1–a2 and a4–a5 of Figure 13 were nearly flat and the lowest SMU traces in panels a3 and a6 (for MPEs at KJPK) increased only slightly.

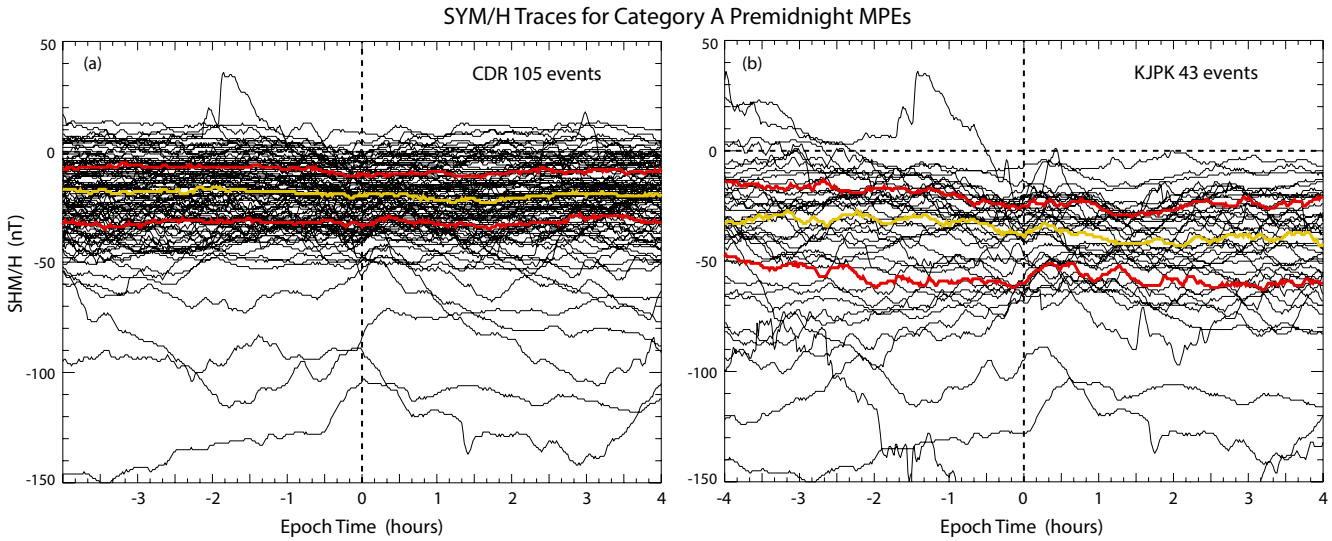

Figure 14. Superposed epoch plots of all SYM/H index values (black traces), the median (yellow traces), and the 25th and 75th percentiles (red traces) as a function of time from 4 h before to 4 h after the time of premidnight category A magnetic perturbation event (MPEs) observed at (a) CDR and (b) KJPK.

Panels a1–a3, b1–b3, and c1–c3 of Figure 13 show that the vast majority of SMU traces for premidnight events were below 200 nT throughout the 8-h periods shown, with only those at and above the 75th percentile in panel a1 exceeding that value within ±30 min of $t = 0$. From −4 to −1 h and +1 to +4 h the median SMU values were relatively constant and 50–100 nT higher in all three premidnight categories at KJPK than at CDR or SALU. The relative scale of increases in SMU panels a1–a3 of Figure 13 was only ∼half as large as the relative scale of decreases in SML in panels a1–a3 of Figure 11, and the relative scale of SMU increases in panels b1–b3 and c1–c3 of Figure 13 was also smaller than those of SML decreases in panels b1–b3 and c1–c3 of Figure 11. The full width–half maximum duration for the premidnight SMU category A medians was ∼60 min, slightly larger than that for SML. Many individual SMU traces were also complex; the fwhm duration of their individual peaks often ranged between 15 and 60 min.

4.2. SYM/H

The SYM/H index (Iyemori et al., 2010), like the older Dst index developed by Sugiura and Poros (1971), describes longitudinally symmetric geomagnetic disturbances at mid-latitudes, but with higher time resolution–1 min versus 1 h (Wanliss & Showalter, 2006).

Figure 14 shows superposed epoch plots of all SYM/H traces and the median, 25th, and 75th percentiles in premidnight category A MPEs observed at CDR and KJPK. Their wide range of values, from ≤−150 to >+30 nT, was typical of those in all categories at all five stations. The pattern of SYM/H traces at CDR shown in Figure 14a was very similar to the category A distributions at RBY, IQA, and SALU (not shown): they were distributed rather uniformly between −40 and +10 nT, with only a small number of traces being below −50 nT. Most of the traces at KJPK were more negative (between 0 and −70 nT) but were not as clearly restricted to a limited range.

Figure S9 shows the medians of SYM/H for all six MLT and time delay categories. Premidnight median values were near −20 nT at the four most poleward stations (panels a1–a4, b1–b4 and c1–c4), but nearer to −30 at KJPK (panels a1, b1, and c1). The medians in most premidnight panels showed temporal variations of up to ±3 nT, but these showed little consistency between stations. The medians for all of the postmidnight MPEs at SALU and KJPK showed a 10–20 nT negative trend before MPE occurrence, were lower (−30–−50 nT) near and after $t = 0$, and showed a comparable rise beginning from 0 to 1 h after MPE occurrence, regardless of delay after substorm onset. The larger short-term variations of the medians in panels b6, b7, c6, and c7 are due to the smaller number of events in these categories. Several of the few postmidnight MPEs at

the three higher latitude stations RBY, CDR, and IQA (not shown) exhibited similar negative trends before MPE occurrence.

5. Discussion and Conclusions

The superposed epoch analysis presented here of upstream solar wind and IMF parameters as well as global geomagnetic indices provides additional evidence of the complexity of circumstances under which large localized magnetic perturbations that can cause GICs can occur.

Our separation of nighttime MPEs into 6 categories based on MLT and time of occurrence after the most recent substorm onset has shown a nearly consistent temporal pattern in only one upstream parameter, the north-south component of the IMF (IMF Bz): most MPEs at all five stations and in all six categories were preceded by drops and rises in the median IMF Bz component ~1 h prior to MPE occurrence. We can thus confirm the findings of two other recent studies that long or even somewhat shorter intervals of southward IMF favored the occurrence of these events. Rogers et al. (2020), using 125 ground-based magnetometers, found that most very large cluster peaks of events with $|dB_H/dt|$ amplitude exceeding the 99.97th percentile at auroral latitudes (55°< MLAT <75°) in the 20–24 h MLT sector occurred during times when IMF Bz was negative, and that occurrences between 3 and 6 MLT were also enhanced under conditions of negative Bz. Dimmock et al. (2020), in a study using 17 years of observations of large dB/dt events recorded in ground magnetometer data obtained by the IMAGE magnetometer network in the Baltic and Fennoscandian region, found that the largest derivatives occurred during times when the IMF Bz component was strongly southward. They linked these conditions to times of substorm activity, but also noted that rapidly varying small-scale currents provided significant contributions to the derivatives of the magnetic field.

Our superposed epoch study did reveal a modest number of individual exceptions to this ~1 h drop and rise pattern in IMF Bz values. However, it is important to note some of the limitations of the OMNI data set, based on solar wind monitoring from spacecraft near the L1 libration point, as reviewed by, for example, Borovsky (2017) and Walsh et al. (2019). First, there are uncertainties in propagation timing from the upstream monitor(s) near the L1 libration point to Earth's magnetosphere; these can be on the order of 10–15 min. These timing variations would act to smooth out small-scale (<15 min) features in the solar wind and IMF that were not temporally correlated with MPE events, and slightly broaden the signatures of features that were temporally correlated with them.

Second, and of more relevance for IMF Bz variations, some solar wind plasma monitored by L1 monitors does not reach the Earth. The solar wind/IMF plasma has a spaghetti-like structure (Borovsky, 2008) that has a transverse scale size relative to the direction of the IMF with medians of 45 R_E (Richardson & Paularena, 2001) or 70 R_E (Borovsky, 2008). Consequently, the large halo orbits of these L1 monitors at times place them more than a scale size away from the Sun-Earth line. These factors, coupled with the directional variability of the solar wind velocity vector, indicate that the observations on which OMNI data are based do not always correspond to the solar wind flux tube(s) that impinge on Earth's magnetosphere. Walsh et al. (2019) and Bier et al. (2014) showed examples during which the measured IMF orientation was significantly different at Wind and ACE and Bier et al. (2014) and Wang et al. (2016) showed better correlations between magnetospheric phenomena (Pc3-4 waves and poleward moving aurora forms, respectively) and IMF measurements from near-Earth solar wind monitors such as THEMIS, Geotail, and Cluster than those measured and time-shifted from the L1 region by Wind and/or ACE. it is thus possible that the small number of intervals of positive IMF Bz identified in our superposed epoch analysis near and shortly before the time of MPEs may be examples of such cases.

Several observational studies have concluded that substorms are often associated with strong localized magnetic perturbations (Ngwira et al., 2015, 2018; Pulkkinen et al., 2003, 2015; Viljanen et al., 2006). Our results concur, to the extent that the majority of MPEs in both MLT ranges (64% and 66%) in our data set occurred within 30 min of a substorm onset (category A), and on average these MPEs occurred close to the times of minima in SML (and by inference close to the times of maxima in nighttime westward electrojets). However, the remaining 34%–36% were much less closely linked to substorms or large-scale electrojets. Negative IMF Bz values also preceded most MPEs that occurred long after the most recent substorm onset, and under conditions when the SML index was much less disturbed. A recent study by Freeman et al. (2019) found a

similar result: In data from 3 stations in the UK over two solar cycles (only) 54%–56% of all extreme rate of change values occurred during substorm expansion or recovery phases.

The consistency with which substorms might drive MPEs was addressed in paper 3, in a comparison of the number of substorm onsets and ≥6 nT/s MPE onsets during 2015 and 2017 between 2330 and 0600 UT (the interval when most of both onsets and MPEs occurred at these five stations) in order to estimate the percentages of substorm onsets after which no MPE occurred within 60 min. These ranged from 75% to 92%, indicating that most substorms were not associated with any large MPEs. Ngwira et al. (2018) came to a similar conclusion: only a small fraction of substorms typically lead to extreme geomagnetic fluctuations. We conclude that although substorm onsets and/or a drop and rise in IMF Bz (based on the OMNI data set) precede many MPE occurrences, and thus have significant predictive value, neither can provide accurate temporal, much less spatial, predictions of all MPE occurrences.

The medians of several other upstream parameters, such as the IMF magnitude, solar wind pressure, and velocity, showed little or no temporal variations during the 8 h before, during, or after MPE occurrence, even though some individual traces were quite large and/or variable. Of these four parameters, the lack of temporal correlation with Psw may seem to be the most surprising, for two reasons. First, there is a well-documented association between interplanetary shocks and sudden impulses (large transient changes in geomagnetic fields on the dayside) and consequent large changes in geomagnetic fields (Araki, 1994; Oliveira & Raeder, 2015; Villante & Piersanti, 2012). However, dayside MPEs, which are often associated with sudden impulses stimulated by large solar wind-induced magnetospheric compressions, were not included in our database. As was noted in paper 3, the nighttime MPE occurrences at each station were compared with the list of interplanetary shocks compiled by Oliveira et al. (2018) in order to identify externally triggered events. Only one nighttime MPE event coincided with a shock event within 30 min, and was removed from our database. The occurrence of EMIC waves also correlates strongly with increases in Psw (e.g., Anderson & Hamilton, 1993; Tetrick et al., 2017; Usanova et al., 2012) and Psw has thus been used to parameterize EMIC wave occurrence in the VERB model (Drozdov et al., 2020). Superposed epoch analyses by Tetrick et al. (2017) showed that even nightside EMIC wave occurrences tended to follow increases in Psw, consistent with event studies by Meurant et al. (2003), Lee et al. (2005, 2007), Zhang et al. (2005, 2008), and Søraas et al. (2013). We speculate that the reason that nightside EMIC waves can be triggered by increases in Psw while nightside MPEs are not is that MPEs are in some way triggered not in the inner magnetosphere but in the magnetotail.

Our superposed epoch analyses of the global SML, SMU, and SYM/H indices have also shown complex temporal relationships to MPE occurrences that in several cases have been anticipated in earlier studies. In a majority of category A events (occurring within 30 min following a substorm onset) minima in SML events coincided within a few min with MPE occurrences (Figures 11 and 12). This may imply either that (a) the current system that causes most premidnight MPEs is the substorm-related westward auroral electrojet, or (b) the process that causes premidnight MPEs tends to occur near the peak of substorm intensity. However, for category B premidnight events there was a time delay of ∼30 min between less well-defined median and 25th and 75th percentile minima in SML and the time of MPE occurrence, and for category C events the medians and 25th and 75th percentiles of SML were nearly flat at CDR and SALU, and their minima in SML at KJPK were weak and occurred even earlier relative to $t = 0$. Thus our grouping of MPEs into categories A, B, and C has both suggested not only a strong connection between SML (and the westward electrojet) for events occurring within 30 min of substorm onset, but also little or no close temporal connection between SML and the smaller number of MPEs in categories B and C. The patterns for categories B and C in particular suggest instead that local rather than more spatially extended increases in ionospheric currents were often associated with these MPE occurrences.

Two recent studies (Huttunen et al., 2002; Pulkkinen et al., 2003) of GIC events that occurred during the April 6–7, 2000 magnetic storm came to conclusions consistent with these patterns: although most of the peak GIC events during the storm were clearly related to substorm intensifications, there were no common characteristics discernible in substorm behavior that could be associated with all the GIC peaks. In particular, both very localized ionospheric current structures (extremely localized and short-lived electrojet activations) and relatively large-scale propagating structures were observed during the peaks in GIC.

Another feature of interest in panels a1–a6 of Figure 11 is the wide range of minima in SML near $t = 0$ for category A events, from below −1,600 nT to −100 nT, even though all of the MPEs included in these panels had large (≥6 nT/s) derivatives. Several earlier studies (e.g., Engebretson, Pilipenko, et al., 2019; Viljanen, 1997; Viljanen et al., 2006) reported a similar lack of good correlation between ΔB and dB/dt amplitudes during large MPEs. This lack can be attributed to two characteristics of the observed MPEs: their short duration relative to the full ΔB excursion, and their greater variability in direction.

The significantly larger range in SML values for postmidnight events than for premidnight events in all three time delay categories (also shown in Figure 11) is more difficult to understand. As Engebretson et al. (2020) suggested in regard to the MPEs associated with an interval of omega bands, it is possible that two separate and highly localized magnetotail–magnetosphere–ionosphere coupling mechanisms may be responsible for generating the large, rapid geomagnetic perturbations that generate premidnight and postmidnight GICs, respectively.

Finally, a wide range of SYM/H values appeared in the individual traces at each station before, during, and after premidnight MPEs. At the 4 most poleward stations their median values were nearly flat (near −20 nT), presumably related to and consistent with quiet or moderate nonstorm conditions when a more contracted oval was overhead. However, in all three time delay categories somewhat more negative median values of SYM/H and gradual decreases before the time of MPE onset and increases afterward were observed at KJPK during premidnight conditions, and during postmidnight conditions somewhat more pronounced decreases and increases were observed at both SALU and KJPK. These lower medians and temporal patterns may be related to conditions when a more expanded auroral oval was overhead, but the mechanisms contributing to the temporal patterns are currently unknown. These observations are consistent with the results shown in Figure 5 of paper 3: although the probability of MPE occurrence for a given range of SYM/H was higher for more negative values, at all 5 stations the total number of MPE occurrences peaked during quiet conditions (SYM/H between −20 and −30 nT).

In regard to the use of geomagnetic indices in general, Kozyreva et al. (2018) noted that the location and timing of large $|dB_H/dt|$ events were not well predicted by geomagnetic index statistics, and Dimmock et al. (2019) noted in their detailed study of magnetic perturbations and GICs during September 7 and 8, 2017 that the peak GIC did not occur during the intervals of the largest depression in the Dst index or of any clear upstream trigger. They noted that unusually large GIC amplitudes could be associated with westward and eastward electrojets, but also that the fine structures of geomagnetic variations which drive GICs are extremely difficult to predict, and further that global geomagnetic indices are not ideal metrics to determine the occurrence or amplitude of GICs.

In summary, the detailed observations presented here provide further evidence of the difficulty in accurately predicting the occurrence of all MPEs and their associated GICs, to say nothing of their specific locations, using observations of external parameters (IMF and solar wind) or global magnetic activity indices. Pulkkinen et al. (2006) reached an even stronger conclusion: although the likelihood of large amplitude fluctuations certainly increases during times of overall geomagnetic activity, "the temporal behavior of the time derivative of the ground magnetic field may not be predictable in a deterministic sense."

Many studies have suggested that mesoscale or small-scale structures in the magnetotail such as bursty bulk flows and dipolarizing flux bundles are closely related to the localized auroral structures associated with many MPEs, but to our knowledge only very recent studies by Nishimura et al. (2020) and Wei et al. (2021) have provided evidence of such relations. It is hoped that future multispacecraft and multimission observational studies will be able to determine whether such a relationship exists, and if so, whether such observations will be able to provide a predictive capability for all or nearly all MPEs and their associated GICs.

Data Availability Statement

MACCS magnetometer data (https://doi.org/10.48322/sydj-ab90) are available in IAGA 2002 ASCII format at http://space.augsburg.edu/maccs/requestdatafile.jsp, AUTUMNX magnetometer data are available in IAGA 2002 ASCII format at http://autumn.athabascau.ca/autumnxquery2.php?year=2015&mon=01&day=01 and CANMOS magnetometer data, provided by the Geological Survey of Canada, are available in

IAGA 2002 ASCII format at http://geomag.nrcan.gc.ca/data-donnee/sd-en.php. GOES 13 magnetometer data are available at https://satdat.ngdc.noaa.gov/sem/goes/data/new_full/. THEMIS auroral imager data are available at the website (http://themis.ssl.berkeley.edu). OMNI solar wind and interplanetary magnetic field data time shifted to the nose of the Earth's bow shock and SYM/H index data are available at the Goddard Space Flight Center Space Physics Data Facility at https://cdaweb.sci.gsfc.nasa.gov/index.html/. The SML and SMU indices are available at http://supermag.jhuapl.edu/indices/, and the SuperMAG substorm database is available online at http://supermag.jhuapl.edu/substorms/. Jesper Gjerloev is SuperMAG Principal Investigator. These SuperMAG products are derived from magnetometer data from INTERMAGNET, Alan Thomson; USGS, Jeffrey J. Love; CARISMA, PI Ian Mann; CANMOS, Geomagnetism Unit of the Geological Survey of Canada; The S-RAMP Database, PI K. Yumoto and Dr. K. Shiokawa; The SPIDR database; AARI, PI Oleg Troshichev; The MACCS program, PI M. Engebretson; GIMA; MEASURE, UCLA IGPP and Florida Institute of Technology; SAMBA, PI Eftyhia Zesta; 210 Chain, PI K. Yumoto; SAMNET, PI Farideh Honary; IMAGE, PI Liisa Juusola; Finnish Meteorological Institute, PI Liisa Juusola; Sodankylä Geophysical Observatory, PI Tero Raita; UiT the Arctic University of Norway, Tromsø Geophysical Observatory, PI Magnar G. Johnsen; GFZ German Research Center For Geosciences, PI Jürgen Matzka; Institute of Geophysics, Polish Academy of Sciences, PI Anne Neska and Jan Reda; Polar Geophysical Institute, PI Alexander Yahnin and Yarolav Sakharov; Geological Survey of Sweden, PI Gerhard Schwarz; Swedish Institute of Space Physics, PI Masatoshi Yamauchi; AUTUMN, PI Martin Connors; DTU Space, PI Dr. Thom R. Edwards and Anna Willer; PENGUIn; South Pole and McMurdo Magnetometer, PIs Louis J. Lanzerotti and Allan T. Weatherwax; ICESTAR; RAPIDMAG; British Antarctic Survey; McMAC, PI Dr. Peter Chi; BGS, PI Dr. Susan Macmillan; Pushkov Institute of Terrestrial Magnetism, Ionosphere and Radio Wave Propagation (IZMIRAN); MFGI, PI B. Heilig; Institute of Geophysics, Polish Academy of Sciences, PI Anne Neska and Jan Reda; and University of L'Aquila, PI M. Vellante; BCMT, V. Lesur and A. Chambodut; Data obtained in cooperation with Geoscience Australia, PI Marina Costelloe; AALPIP, co-PIs Bob Clauer and Michael Hartinger; SuperMAG, Data obtained in cooperation with the Australian Bureau of Meteorology, PI Richard Marshall.

Acknowledgments
This research was supported by NSF grants AGS-1651263 and AGS-2013648 to Augsburg University, AGS-1654044 and AGS-2013433 to the University of Michigan, PLR-1543364, AGS2027210, and AGS-2027168 to Virginia Tech, and at UCLA by the MMS project. Martin G. Connors thanks NSERC for research support and the Canadian Space Agency for support of AUTUMNX. The spherical elementary currents produced by James M. Weygand were made possible by NASA grants 80NSSC18K1220, 80NSSC18K1227, 80NSSC20K1364, 80NSSC18K0570, and NASA Contract 80GSFC17C0018.

References

Anderson, B. J., & Hamilton, D. C. (1993). Electromagnetic ion cyclotron waves stimulated by modest magnetospheric compressions. *Journal of Geophysical Research*, *98*, 11369–11382. https://doi.org/10.1029/93JA00605

Apatenkov, S. V., Pilipenko, V. A., Gordeev, E. I., Viljanen, A., Juusola, L., Belakhovsky, V. B., et al. (2020). Auroral omega bands are a significant cause of large geomagnetically induced currents. *Geophysical Research Letters*, *47*, e2019GL086677. https://doi.org/10.1029/2019GL086677

Araki, T. (1994). A physical model of the geomagnetic sudden commencement, in solar wind sources of magnetospheric ultra-low-frequency waves. In M. J. Engebretson, K. Takahashi, & M. Scholer (Eds.), Geophysical. Monograph series (Vol. 81, pp. 183–200). https://doi.org/10.1029/GM081p0183

Belakhovsky, V. B., Sakharov, Y. A., Pilipenko, V. A., & Selivanov, V. N. (2018). Characteristics of the variability of a geomagnetic field for studying the impact of the magnetic storms and substorms on electrical energy systems, Izvestiya. *Physics of the Solid Earth*, *54*, 52–65. https://doi.org/10.1134/S1069351318010032

Bier, E. A., Owusu, N., Engebretson, M. J., Posch, J. L., Lessard, M. R., & Pilipenko, V. A. (2014). Investigating the IMF cone angle control of Pc3-4 pulsations observed on the ground. *Journal of Geophysical Research: Space Physics*, *119*, 1797–1813. https://doi.org/10.1002/2013JA019637

Borovsky, J. E. (2008). Flux tube texture of the solar wind: Strands of the magnetic carpet at 1 AU? *Journal of Geophysical Research*, *113*, A08110. https://doi.org/10.1029/2007JA012684

Borovsky, J. E. (2017). The spatial structure of the oncoming solar wind at Earth and the shortcomings of a solar wind monitor at L1. *Journal of Atmospheric and Solar-Terrestrial Physics*, *177*, 2–11. https://doi.org/10.1016/j.jastp.2017.03.014

Boteler, D. H. (2001). Assessment of geomagnetic hazard to power systems in Canada. *Natural Hazards*, *23*, 101–120. https://doi.org/10.1023/A:1011194414259

Boteler, D. H. (2019). A 21st century view of the March 1989 magnetic storm. *Space Weather*, *17*, 1427–1441. https://doi.org/10.1029/2019SW002278

Boteler, D. H., Pirjola, R. J., & Nevanlinna, H. (1998). The effects of geomagnetic disturbances on electrical systems at the Earth's surface. *Advances in Space Research*, *22*, 17–27. https://doi.org/10.1016/S0273-1177(97)01096-X

Carrington, R. C. (1859). Description of a singular appearance seen in the Sun on September 1. *Monthly Notices of the Royal Astronomical Society*, *20*, 13–15. https://doi.org/10.1093/mnras/20.1.13

Chree, C. (1913). Some phenomena of sunspots and of terrestrial magnetism at Kew observatory. *Philosophical Transactions of the Royal Society of London. Series A*, *212*, 75–116. https://doi.org/10.1098/rsta.1913.0003

Connors, M., Schofield, I., Reiter, K., Chi, P. J., Rowe, K. M., & Russell, C. T. (2016). The AUTUMNX magnetometer meridian chain in Québec, Canada. *Earth Planets and Space*, *68*. https://doi.org/10.1186/s40623-015-0354-4

Dimmock, A. P., Rosenqvist, L., Hall, J.-O., Viljanen, A., Yordanova, E., Honkonen, I., et al. (2019). The GIC and geomagnetic response over Fennoscandia to the 7–8 September 2017 geomagnetic storm. *Space Weather*, *17*, 989–1010. https://doi.org/10.1029/2018SW002132

Dimmock, A. P., Rosenqvist, L., Welling, D. T., Viljanen, A., Honkonen, I., Boynton, R. J., & Yordanova, E. (2020). On the regional variability of dB/dt and its significance to GIC. *Space Weather*, *18*, e2020SW002497. https://doi.org/10.1029/2020SW002497

Drozdov, A. Y., Usanova, M. E., Hudson, M. K., Allison, H. J., & Shprits, Y. Y. (2020). The role of hiss, chorus, and EMIC waves in the modeling of the dynamics of the multi-MeV radiation belt electrons. *Journal of Geophysical Research: Space Physics*, *125*, e2020JA028282. https://doi.org/10.1029/2020JA028282

Engebretson, M. J., Hughes, W. J., Alford, J. L., Zesta, E., Cahill, L. J., Jr., Arnoldy, R. L., & Reeves, G. D. (1995). Magnetometer array for cusp and cleft studies observations of the spatial extent of broadband ULF magnetic pulsations at cusp/cleft latitudes. *Journal of Geophysical Research*, *100*, 19371–19386. https://doi.org/10.1029/95JA00768

Engebretson, M. J., Kirkevold, K. R., Steinmetz, E. S., Pilipenko, V. A., Moldwin, M. B., McCuen, B. A., et al. (2020). Interhemispheric comparisons of large nighttime magnetic perturbation events relevant to GICs. *Journal of Geophysical Research: Space Physics*, *125*, e2020JA028128. https://doi.org/10.1029/2020JA028128

Engebretson, M. J., Pilipenko, V. A., Ahmed, L. Y., Posch, J. L., Steinmetz, E. S., Moldwin, M. B., et al. (2019a). Nighttime magnetic perturbation events observed in Arctic Canada: 1. Survey and statistical analysis. *Journal of Geophysical Research: Space Physics*, *124*, 7442–7458. https://doi.org/10.1029/2019JA026794

Engebretson, M. J., Pilipenko, V. A., Steinmetz, E. S., Moldwin, M. B., Connors, M. G., Boteler, D. H., et al. (2021). Nighttime magnetic perturbation events observed in Arctic Canada: 3. Occurrence and amplitude as functions of magnetic latitude, local time, and magnetic disturbances. *Space Weather*, *19*, e2020SW002526. https://doi.org/10.1029/2020SW002526

Engebretson, M. J., Steinmetz, E. S., Posch, J. L., Pilipenko, V. A., Moldwin, M. B., Connors, M. G., et al. (2019b). Nighttime magnetic perturbation events observed in Arctic Canada: 2. Multiple- instrument observations. *Journal of Geophysical Research: Space Physics*, *124*, 7459–7476. https://doi.org/10.1029/2019JA026797

Freeman, M. P., Forsyth, C., & Rae, I. J. (2019). The influence of substorms on extreme rates of change of the surface horizontal magnetic field in the United Kingdom. *Space Weather*, *17*, 827–844. https://doi.org/10.1029/2018SW002148

Frey, H. U., Mende, S. B., Angelopoulos, V., & Donovan, E. F. (2004). Substorm onset observations by IMAGE-FUV. *Journal of Geophysical Research*, *109*, A10304. https://doi.org/10.1029/2004JA010607

Hapgood, M. (2019). The great storm of May 1921: An exemplar of a dangerous space weather event. *Space Weather*, *17*, 950–975. https://doi.org/10.1029/2019SW002195

Honkonen, I., Kuvshinov, A., Rastätter, L., & Pulkkinen, A. (2018). Predicting global ground geoelectric field with coupled geospace and three-dimensional geomagnetic induction models. *Space Weather*, *16*, 1028–1041. https://doi.org/10.1029/2018SW001859

Huttunen, K. E. J., Koskinen, H. E. J., Pulkkinen, T. I., Pulkkinen, A., Palmroth, M., Reeves, E. G. D., & Singer, H. J. (2002). April 2000 magnetic storm: Solar wind driver and magnetospheric response. *Journal of Geophysical Research*, *107*, 1440–1. https://doi.org/10.1029/2001JA009154

Iyemori, T., Takeda, M., Nose, M., Odagi, Y., & Toh, H. (2010). *Mid-latitude geomagnetic indices ASY and SYM for 2009 (provisional), internal report of data analysis center for geomagnetism and space magnetism*. Kyoto University.

Knipp, D. J. (2015). Synthesis of geomagnetically induced currents: Commentary and research. *Space Weather*, *13*, 727–729. https://doi.org/10.1002/2015SW001317

Knipp, D. J., & Gannon, J. L. (2019). The 2019 National Space Weather strategy and action plan and beyond. *Space Weather*, *17*, 794–795. https://doi.org/10.1029/2019SW002254

Kozyreva, O. V., Pilipenko, V. ,A., Belakhovsky, V. B., & Sakharov, Y. ,A. (2018). Ground geomagnetic field and GIC response to March 17, 2015, storm. *Earth, Planets, and Space*, *70*, 157. https://doi.org/10.1186/s40623-018-0933-2

Lee, D.-Y., Lyons, L. R., & Reeves, G. D. (2005). Comparison of geosynchronous energetic particle flux responses to solar wind dynamic pressure enhancements and substorms. *Journal of Geophysical Research*, *110*, A09213. https://doi.org/10.1029/2005JA011091

Lee, D.-Y., Ohtani, S., Brandt, P. C., & Lyons, L. R. (2007). Energetic neutral atom response to solar wind dynamic pressure enhancements. *Journal of Geophysical Research*, *112*, A09210–n. https://doi.org/10.1029/2007JA012399

Love, J. J., Hayakawa, H., & Cliver, E. W. (2019). Intensity and impact of the New York Railroad superstorm of May 1921. *Space Weather*, *17*, 1281–1292. https://doi.org/10.1029/2019SW002250

Lühr, H., Rother, M., Iyemori, T., Hansen, T. L., & Lepping, R. P. (1998). Superposed epoch analysis applied to large-amplitude travelling convection vortices. *Annals of Geophysics*, *16*, 743–753. https://doi.org/10.1007/s00585-998-0743-0

Marshalko, E., Kruglyakov, M., Kuvshinov, A., Juusola, L., Kwagala, N. K., Sokolova, E., & Pilipenko, V. (2021). Comparing three approaches to the inducing source setting for the ground electromagnetic field modeling due to space weather events. *Space Weather*, *19*, e2020SW002657. https://doi.org/10.1029/2020SW002657

Meurant, M., Gérard, J.-C., Hubert, B., Coumans, V., Blockx, C., Østgaard, N., & Mende, S. B. (2003). Dynamics of global scale electron and proton precipitation induced by a solar wind pressure pulse. *Geophysical Research Letters*, *30*, 2032. https://doi.org/10.1029/2003GL018017

Mukhopadhyay, A., Welling, D. T., Liemohn, M. W., Ridley, A. J., Chakraborty, S., & Anderson, B. J. (2020). Conductance Model for Extreme Events: Impact of auroral conductance on space weather forecasts. *Space Weather*, *18*, e2020SW002551. https://doi.org/10.1029/2020SW002551

Newell, P. T., & Gjerloev, J. W. (2011). Evaluation of SuperMAG auroral electrojet indices as indicators of substorms and auroral power. *Journal of Geophysical Research*, *116*, A12211. https://doi.org/10.1029/2011JA016779

Ngwira, C. M., & Pulkkinen, A. A. (2019). An introduction to geomagnetically induced currents (2019). In J. L. Gannon, A. Swidinsky, & Z. Xu (Eds.), Geomagnetically induced currents from the Sun to the power grid, geophysical monograph series (Vol. 244, pp. 3–13). American Geophysical Union. https://doi.org/10.1002/9781119434412.ch1

Ngwira, C. M., Pulkkinen, A. A., Bernabeu, E., Eichner, J., Viljanen, A., & Crowley, G. (2015). Characteristics of extreme geoelectric fields and their possible causes: Localized peak enhancements. *Geophysical Research Letters*, *42*, 6916–6921. https://doi.org/10.1002/2015GL065061

Ngwira, C. M., Sibeck, D. G., Silveira, M. D. V., Georgiou, M., Weygand, J. M., Nishimura, Y., & Hampton, D. (2018). A study of intense local d*Bdt* variations during two geomagnetic storms. *Space Weather*, *16*, 676–693. https://doi.org/10.1029/2018SW001911

Nikitina, L., Trichtchenko, L., & Boteler, D. H. (2016). Assessment of extreme values in geomagnetic and geoelectric field variations for Canada. *Space Weather*, *14*, 481–494. https://doi.org/10.1002/2016SW001386

Nishimura, Y., Lyons, L. R., Gabrielse, C., Sivadas, N., Donovan, E. F., Varney, R. H., et al. (2020). Extreme magnetosphere-ionosphere-thermosphere responses to the 5 April 2010 Supersubstorm. *Journal of Geophysical Research: Space Physics*, *125*(4), A09218. https://doi.org/10.1029/2019JA027654

Oliveira, D. M., Arel, D., Raeder, J., Zesta, E., Ngwira, C. M., Carter, B. A., et al. (2018). Geomagnetically induced currents caused by interplanetary shocks with different impact angles and speeds. *Space Weather*, *16*, 636–647. https://doi.org/10.1029/2018SW001880

Oliveira, D. M., & Raeder, J. (2015). Impact angle control of interplanetary shock geoeffectiveness: A statistical study. *Journal of Geophysical Research: Space Physics*, *120*, 4313–4323. https://doi.org/10.1002/2015JA021147

Pulkkinen, A., Bernabeu, E., Eichner, J., Viljanen, A., & Ngwira, C. M. (2015). Regional-scale high-latitude extreme geoelectric fields pertaining to geomagnetically induced currents. *Earth Planets and Space*, *67*. https://doi.org/10.1186/s40623-015-0255-6

Pulkkinen, A., Klimas, A., Vassiliadis, D., Uritsky, V., & Tanskanen, E. (2006). Spatiotemporal scaling properties of the ground geomagnetic field variations. *Journal of Geophysical Research*, *111*, A03305. https://doi.org/10.1029/2006JA01129410.1029/2005ja011294

Pulkkinen, A., Thomson, A., Clarke, E., & McKay, A. (2003). April 2000 geomagnetic storm: Ionospheric drivers of large geomagnetically induced currents. *Annales Geophysicae*, *21*(3), 709–717. https://doi.org/10.5194/angeo-21-709-2003

Richardson, J. D., & Paularena, K. I. (2001). Plasma and magnetic field correlations in the solar wind. *Journal of Geophysical Research*, *106*, 239–251. https://doi.org/10.1029/2000JA000071

Rogers, N. C., Wild, J. A., Eastoe, E. F., Gjerloev, J. W., Thomson, A. W. P., & Thomson, A. W. P. (2020). A global climatological model of extreme geomagnetic field fluctuations. *Journal of Space Weather and Space Climate*, *10*, 5. https://doi.org/10.1051/swsc/2020008

Søraas, F., Laundal, K. M., & Usanova, M. (2013). Coincident particle and optical observations of nightside subauroral proton precipitation. *Journal of Geophysical Research: Space Physics*, *118*, 1112–1122. https://doi.org/10.1002/jgra.50172

Sugiura, M., & Poros, D. J. (1971). *Hourly values of equatorial Dst for years 1957 to 1970, Rep. X-645-71-278*. Goddard Space Flight Center.

Tetrick, S. S., Engebretson, M. J., Posch, J. L., Olson, C. N., Smith, C. W., Denton, R. E., et al. (2017). Location of intense electromagnetic ion cyclotron (EMIC) wave events relative to the plasmapause: Van Allen Probes observations. *Journal of Geophysical Research: Space Physics*, *122*, 4064–4088. https://doi.org/10.1002/2016JA023392

Usanova, M. E., Mann, I. R., Bortnik, J., Shao, L., & Angelopoulos, V. (2012). THEMIS observations of electromagnetic ion cyclotron wave occurrence: Dependence on AE, SYMH, and solar wind dynamic pressure. *Journal of Geophysical Research*, *117*, A10218. https://doi.org/10.1029/2012JA018049

Viljanen, A. (1997). The relation between geomagnetic variations and their time derivatives and implications for estimation of induction risks. *Geophysical Research Letters*, *24*, 631–634. https://doi.org/10.1029/97GL00538

Viljanen, A., Nevanlinna, H., Pajunpää, K., & Pulkkinen, A. (2001). Time derivative of thehorizontal geomagnetic field as an activity indicator. *Annales Geophysicae*, *19*, 1107–1118. https://doi.org/10.5194/angeo-19-1107-2001

Viljanen, A., & Tanskanen, E. (2011). Climatology of rapid geomagnetic variations at high latitudes over two solar cycles. *Annales Geophysicae*, *29*, 1783–1792. https://doi.org/10.5194/angeo-29-1783-2011

Viljanen, A., Tanskanen, E. I., & Pulkkinen, A. (2006). Relation between substorm characteristics and rapid temporal variations of the ground magnetic field. *Annales Geophysicae*, *24*, 725–733. https://doi.org/10.5194/angeo-24-725-2006

Villante, U., & Piersanti, M. (2012). Sudden Impulses in the Magnetosphere and at Ground. In M. Lazar, & IntechOpen (Eds.), *Sudden impulses in the magnetosphere and at ground, exploring the solar wind* (pp. 399–416). https://doi.org/10.5772/36770

Vorobev, A. V., Pilipenko, V. A., Sakharov, Y. A., & Selivanov, V. N. (2019). Statistical relationships between variations of the geomagnetic field, auroral electrojet and geomagnetically induced currents. *Solar-Terrestrial Physics*, *5*(1), 35–42. https://doi.org/10.12737/stp-51201905

Walsh, B. M., Bhakyapaibul, T., & Zou, Y. (2019). Quantifying the uncertainty of using solar wind measurements for geospace inputs. *Journal of Geophysical Research: Space Physics*, *124*, 3291–3302. https://doi.org/10.1029/2019JA026507

Wang, B., Nishimura, Y., Zou, Y., Lyons, L. R., Angelopoulos, V., Frey, H., & Mende, S. (2016). Investigation of triggering of poleward moving auroral forms using satellite-imager coordinated observations. *Journal of Geophysical Research: Space Physics*, *121*, 10929–10941. https://doi.org/10.1002/2016JA023128

Wanliss, J. A., & Showalter, K. M. (2006). High-resolution global storm index: Dst versus SYM- H. *Journal of Geophysical Research*, *111*, A02202. https://doi.org/10.1029/2005JA011034

Wei, D., Dunlop, M. W., Yang, J., Dong, X., Yu, Y., & Wang, T. (2021). Intense *dB/dt* variations driven by near-Earth bursty bulk flows (BBFs): A case study. *Geophysical Research Letters*, *48*, e2020GL091781. https://doi.org/10.1029/2020GL091781

Welling, D. T., Love, J. J., Rigler, E. J., Oliveira, D. M., Komar, C. M., & Morley, S. K. (2020). Numerical simulations of the geospace response to the arrival of an idealized perfect interplanetary coronal mass ejection. *Space Weather*, *18*. https://doi.org/10.1029/2020SW002489

Wintoft, P., Wik, M., & Viljanen, A. (2015). Solar wind driven empirical forecast models of the time derivative of the ground magnetic field. *Journal of Space Weather and Space Climate*, *5*(A7). https://doi.org/10.1051/swsc/2015008

Woodroffe, J. R., Morley, S. K., Jordanova, V. K., Henderson, M. G., Cowee, M. M., & Gjerloev, J. (2016). The latitudinal variation of geoelectromagnetic disturbances during large (*Dst*≤−100 nT) geomagnetic storms. *Space Weather*, *14*, 668–681. https://doi.org/10.1002/2016SW001376

Yagova, N. V., Pilipenko, V. A., Fedorov, E. N., Lhamdon-tong, A. D., & Gusev, Y. P. (2018). Geomagnetically induced currents and space weather: Pi3 pulsations and extreme values of the time derivatives of the horizontal components of the geomagnetic field, *Izvestiya*. *Physics of the Solid Earth*, *54*, 749–763. https://doi.org/10.1134/S1069351318050130

Zhang, Y., Paxton, L. J., & Zheng, Y. (2008). Interplanetary shock induced ring current auroras. *Journal of Geophysical Research*, *113*, A01212. https://doi.org/10.1029/2007JA012554

Zhang, Y., Paxton, L., Morrison, D., Wolven, B., Kil, H., & Wing, S. (2005). Nightside detached auroras due to precipitating protons/ions during intense magnetic storms. *Journal of Geophysical Research*, *110*, A02206. https://doi.org/10.1029/2004JA010498